Chemical Engineering Journal 532 (2026) 174527

Contents lists available at ScienceDirect

Chemical Engineering Journal

journal homepage: www.elsevier.com/locate/cej

# Controlled exsolution-dissolution in double perovskites enables symmetrical-capable high-performance SOFC electrodes

Jakub Lach [a], Kun Zheng [a,b,*], Cristian Radu [c], Marcin Kryński [d], Michał Gogacz [a], Yihan Ling [e], Alicja Klimkowicz [f], Marcin Łapiński [g]

[a] Department of Hydrogen Energy, Faculty of Energy and Fuels, AGH University of Krakow, al. A. Mickiewicza 30, 30-059, Krakow, Poland
[b] AGH Centre of Energy, AGH University of Krakow, ul. Czarnowiejska 36, 30-054, Krakow, Poland
[c] National Institute of Materials Physics, Atomistilor 405A, 077125, Magurele, Romania
[d] Faculty of Physics, Warsaw University of Technology, 00-662, Warsaw, Poland
[e] School of Materials Science and Physics, China University of Mining and Technology, Xuzhou, Jiangsu Province, 221116, PR China
[f] College of Engineering, Shibaura Institute of Technology, 3-7-5 Toyosu, Koto City, 135-8548, Tokyo, Japan
[g] Institute of Nanotechnology and Materials Engineering, Faculty of Applied Physics and Mathematics, Gdansk University of Technology, ul. Gabriela Narutowicza 11/12, 80-233, Gdańsk, Poland

ARTICLE INFO

*Keywords:*
Multi-elemental exsolution
Core–shell nanostructures
Nanofiber perovskites
Exsolved nano-oxides for air electrodes
Symmetrical electrodes

ABSTRACT

*In situ* exsolution has emerged as a powerful strategy for tailoring fuel electrode catalysts in solid oxide fuel cells (SOFCs), yet its integration with reversible exsolution-dissolution processes and its application to symmetrical-capable electrode design remain largely unexplored. Here, we demonstrate controlled exsolution-dissolution in nanofiber double perovskites as a rational route to engineer high-performance SOFC electrodes operable in both symmetrical and anode-supported configurations. $Sm_{0.9}Ba_{0.9}Mn_{1.8-x}Fe_xCo_{0.1}Ni_{0.1}O_{5+\delta}$ nanofiber perovskites enable composition-dependent control of nanoparticle evolution. Under reducing conditions, socketed Co–Ni–Fe alloy nanocatalysts exsolve and partially embed into the perovskite lattice, while oxidation induces their transformation into $Fe_{3-x-y}Ni_xCo_yO_4$-type hollow core–shell nano-oxides *via* a Kirkendall-type mechanism. The nanofiber architecture promotes smaller and more densely distributed nanoparticles compared to powders, enhancing catalytic activity and redox stability. The optimized composite electrode delivers a low polarization resistance of 0.046 Ω $cm^2$ at 800 °C. Anode-supported cells achieve a peak power density of 1112 mW $cm^{-2}$ at 850 °C and 877 mW $cm^{-2}$ at 800 °C, while symmetrical cells deliver 816 mW $cm^{-2}$ at 800 °C with stable operation. This work establishes controlled exsolution-dissolution as a versatile platform for designing symmetrical-capable high-performance SOFC electrodes and highlights hollow core–shell nanostructure engineering as a powerful strategy for durable solid oxide electrochemical systems.

## 1. Introduction

The ongoing global energy transition is driving an increasing share of electricity generation from renewable sources. However, the intermittent nature of solar and wind power necessitates the development of efficient energy conversion and storage systems. In this context, Solid Oxide Fuel Cells (SOFCs) have gained significant attention as promising technologies for sustainable and efficient energy utilization [1–7]. SOFCs remain a major focus of research, with continuous efforts directed toward enhancing power density, durability, and cost-effectiveness through the design of high-performance electrode materials [8–10]. Among these, symmetrical SOFCs (S-SOFCs) employing identical electrode materials have attracted considerable interest due to various advantages, including simplified fabrication processes, reduced manufacturing costs, and mitigation of chemical and thermomechanical incompatibility problems between the electrolyte and electrodes [2–7,11–15]. However, to ensure high conversion efficiency and long operational lifetime of S-SOFCs, redox-stable electrode materials with mixed ionic-electronic conductivity and high electrocatalytic activity for hydrogen oxidation and oxygen reduction are crucial [2–7]. Mn-based perovskite oxides have emerged as promising S-SOFC electrode candidates owing to their redox stability and catalytic activity [2–7,16].

* Corresponding author at: Department of Hydrogen Energy, Faculty of Energy and Fuels, AGH University of Krakow, al. A. Mickiewicza 30, 30-059, Krakow, Poland.
*E-mail address:* zheng@agh.edu.pl (K. Zheng).

https://doi.org/10.1016/j.cej.2026.174527
Received 1 December 2025; Received in revised form 17 February 2026; Accepted 22 February 2026
Available online 23 February 2026

Representative examples include $NdBaMn_2O_{5+\delta}$ [11], $La_{0.8}Ba_{0.2}MnO_3$ [12], $SmBaMn_2O_{5+\delta}$ [5], and $PrBaMn_2O_{5+\delta}$ [17]. Furthermore, Mn-based double perovskites, such as $BaLnMn_2O_{5+\delta}$ (Ln = Pr, Nd, Sm, Gd, Dy, Er, Y) [18,19], $BaY_{1-x}Pr_xMn_2O_{5+\delta}$ [20], and $BaGd_{1-x}Yb_xMn_2O_{5+\delta}$ [21], exhibit excellent oxygen transport properties and redox stability, making them attractive as SOFC electrodes and oxygen storage materials [18–21].

Perovskites with Mn in the B-site sublattice are catalytically active in oxygen-involving reactions and can simultaneously serve as support for exsolved nanocatalysts [2,20,22]. Their layered crystal structure, composed of alternating lanthanide and alkaline-earth metal planes, weakens oxygen bonds and creates channels for efficient oxygen-ion migration, thereby enhancing ionic conductivity [23,24]. However, Mn-based perovskites are prone to cation segregation and secondary phase formation, with impurities such as $BaMnO_3$, $Sm_2O_3$, and MnO frequently reported in $Ln_{0.5}Ba_{0.5}MnO_{3-\delta}$ (Ln = La, Pr, Nd, Sm) compositions [4,16,22,25]. Partial substitution of Mn with Fe effectively stabilizes the perovskite structure and suppresses phase segregation [16]. Consequently, perovskite oxides co-utilizing Mn and Fe on the B-site have been widely explored as electrode materials for solid oxide cells [13,26–28]. Representative examples include $La_{0.6}Sr_{0.4}Mn_{0.2}Fe_{0.8}O_{3-\delta}$ [26], $Pr_{0.6}Sr_{0.4}Mn_{0.2}Fe_{0.7}Ni_{0.1}O_{3-\delta}$ [13], and $La_{0.6}Sr_{0.2}Ba_{0.2}Mn_{0.2}Fe_{0.8}O_3$ [27], in which *in situ* exsolution of Fe- or Fe-Ni-based nanoparticles has been demonstrated under reducing atmospheres, yielding enhanced electrode activity. Beyond structural stabilization, the coexistence of Fe and Mn in different oxidation states is expected to facilitate electronic conductivity, thereby contributing to the superior electrode performance [26]. Interestingly, incorporating metals that can be reduced to the metallic state into the perovskite B-sublattice may enable surface decoration with metallic nanoparticles *via in situ* exsolution under reducing conditions. These exsolved nanoparticles not only enhance electrocatalytic activity but also improve electrode stability [29]. Moreover, exsolution-generated nanocatalysts can substantially expand the effective triple-phase boundary region and accelerate electrode reaction kinetics [13]. For instance, Qin et al. reported that *in situ* exsolved $Fe_{0.7}Ru_{0.3}$-core/$FeO_x$-shell nanocatalysts anchored on the $(Pr_{0.5}Sr_{0.5})_{0.9}Fe_{0.8}Ru_{0.1}Nb_{0.1}O_{3-\delta}$ perovskite exhibited excellent electrocatalytic activity toward $H_2$ and $C_3H_8$ oxidation, along with improved electrode stability [30]. Hou et al. developed $La_{0.5}Ba_{0.5}Mn_{0.8}Co_{0.1}Fe_{0.1}O_{3-\delta}$ fuel electrodes and found that *in situ* exsolved $Co_{0.94}Fe_{0.06}$-core/$(Co,Fe)_3O_4$-shell nanoparticles significantly enhanced catalytic activity of the SOFC anode [16]. Similarly, *in situ* exsolution of highly active NiFe-core /$FeO_x$-shell nanoparticles from $Pr_{0.4}Sr_{1.6}(NiFe)_{1.5}Mo_{0.5}O_{6-\delta}$ double perovskite concurrently generates oxygen vacancies, thereby improving $CO_2$ adsorption and electrolysis processes [31]. Kim et al. found that surfaces decorated with Co nanoparticles exsolved from $Pr_{0.5}Ba_{0.5}Mn_{0.85}Co_{0.15}O_{3-\delta}$ showed better catalytic activity for CO oxidation than the Co-doped compound without exsolved nanocatalysts [32]. Therefore, *in situ* exsolution has been reported as an interesting way to improve electrocatalytic properties and redox-stability in perovskite oxides [14,16,29,30,33–42] and the benefits of this process are difficult to achieve with other preparation methods [43]. Moreover, the reversibility of the exsolution process can mitigate nanoparticle agglomeration and carbon deposition, enhancing fuel flexibility when hydrocarbons are used as fuels [2,29].

While *in situ* exsolution is well established for fuel electrodes, its application in air electrodes remains very limited. For instance, *in situ* exsolution of $Co_3O_4$ nanocatalysts on the $Ca_{3-x}Co_4O_{9+\delta}$ air electrode enabled a ~ 60% reduction in polarization resistance (Rp) at 800 °C, achieving 0.09 Ω $cm^2$. Owing to the increased number of electrochemically active sites on the cathode, the anode-supported cell achieved a peak power density (1069 mW $cm^{-2}$) more than twice that of the cell without the exsolved phase [10]. In turn, $Pr_{0.2}Ba_{0.8}Co_{0.7}Fe_{0.3}O_{3-\delta}$ air electrode modified by voltage-driven *in situ* exsolved CoO nanoparticles exhibited the Rp approximately 1/3 of that for the pristine cathode [9]. As the cathodic reaction is typically the rate-limiting step for the overall intermediate- and low-temperature SOFC performance [44], the decoration of the air electrode surface with nanocatalysts emerges as a particularly promising strategy.

The capability of *in situ* exsolution to be employed in both anodes and cathodes makes this process a particularly attractive approach for tailoring electrode properties in S-SOFCs. Zhang et al. exploited this concept and demonstrated that Co nanocatalysts exsolved from $Sm_{0.9}Ba_{0.9}Mn_{1.8}Co_{0.2}O_{5+\delta}$ significantly promoted the rate-limiting steps in the hydrogen oxidation process, whereas oxidized $Co_3O_4$ nanoparticles enhance oxygen reduction activity, when the material is used as an electrode in S-SOFCs [2].

Electrode morphology is another critical factor for SOFC performance. Nanofiber perovskite electrodes have been reported and shown to deliver high electrochemical activity [2,9,10,14,16,30–42,45]. In addition, nanofiber electrodes are typically sintered at relatively low temperatures, usually in the range of 800–900 °C, to preserve their favorable fibrous morphology [46–49]. For example, Kim et al. showed that 8YSZ nanofiber electrodes sintered at 800 °C maintained substantially higher specific surface area and oxygen vacancy concentration than those sintered at 1200 °C, resulting in markedly enhanced electrochemical performance [50]. However, studies on nanofibers with *in situ* exsolution remain limited. Moreover, rigorous comparisons between nanofibrous and powder electrodes under identical compositions and operating conditions are scarce, and the implementation of nanofiber-based exsolution concepts in symmetrical SOFCs has only rarely been explored.

Most previous work has focused on mono- or bimetallic exsolved nanoparticles and has not established a systematic strategy to control nanoparticle density, size, and morphology within nanofibrous architectures. Compared with conventional bimetallic systems, trimetallic exsolved nanoparticles can offer enhanced catalytic activity and stability by combining entropic and kinetic advantages [29,42,51]. In this context, Fe substitution enables precise tuning of *in situ* exsolution kinetics and leads to the formation of hollow core–shell nanocatalysts with a highly favorable morphology. Notably, the formation of the hollow core–shell nanooxide is consistent with a Kirkendall-type mechanism, in which strongly asymmetric cation diffusion during oxidation drives vacancy accumulation and void nucleation within the nanoparticles, ultimately yielding hollow core–shell structures [52–54]. This mechanism enables the formation of polycrystalline nanoparticles with a high density of grain boundaries, which can act as catalytically active sites for electrochemical reactions [55]. Moreover, the hollow core–shell architecture can enhance electrode functionality by shortening mass-transport pathways across the shell and increasing the density of accessible active sites, while the internal void provides a mechanical "buffer space" that helps accommodate redox-induced strain during oxidation and reduction cycling [53]. Because exsolution is governed not only by reducible cation substitution but also by lattice–surface equilibrium, A-site deficiency was introduced to facilitate uniform nanoparticle formation and promote self-exsolution under reducing conditions [2,56–60].

Based on this understanding, the present work aims to develop redox-stable, high-performance electrodes for S-SOFCs. The A-site cations were selected to provide a double perovskite structure with favorable oxygen-ion transport. Concurrently, the B-site cations were chosen to ensure a stable structure in both air and $H_2$-containing atmospheres. Co and Ni were incorporated for their ability to undergo electrochemical reduction at SOFC operating temperatures, forming highly active metallic nanocatalysts on the surface [33]. The substitution of Fe for Mn in $Sm_{0.9}Ba_{0.9}Mn_{1.8-x}Fe_xCo_{0.1}Ni_{0.1}O_{5+\delta}$ oxide was employed to stabilize a single-phase double-perovskite framework and to enable reversible, atmosphere-dependent nanocatalyst evolution [16]. Under reducing conditions (hydrogen electrode) it yields a dense dispersion of socketed ternary Fe–Co–Ni alloy nanoparticles, whereas under oxidizing conditions (air electrode) it promotes the formation of hollow core–shell spinel oxide nanocatalysts. The fabricated nanofibrous electrodes

markedly promote the *in situ* exsolution of smaller and more densely distributed nanoparticles compared with the corresponding powders, thereby greatly enhancing electrocatalytic activity. The air electrode decorated with hollow core–shell nanocatalysts enabled an anode-supported cell to achieve a peak power density of 1112 mW $cm^{-2}$ at 850 °C, and 877 mW $cm^{-2}$ at 800 °C, maintaining stable operation for 200 h. Furthermore, the S-SOFC with *in situ* exsolved nanoparticles delivered an exceptional 816 mW $cm^{-2}$ at 800 °C. These findings establish a new design paradigm for S-SOFCs, integrating multi-elemental *in situ* exsolution within nanofibrous double-perovskite electrodes to synergistically enhance both fuel and air electrode performance, paving the way for next-generation energy conversion systems.

## 2. Results and discussion

### 2.1. Structural properties and microstructure of $Sm_{0.9}Ba_{0.9}Mn_{1.8-x}Fe_xCo_{0.1}Ni_{0.1}O_{5+\delta}$

Single-phase $Sm_{0.9}Ba_{0.9}Mn_{1.8-x}Fe_xCo_{0.1}Ni_{0.1}O_{5+\delta}$ (x = 0, 0.45, and 0.9) nanofibers crystallize in the tetragonal $P4/nmm$ space group (No. 129), as confirmed by the XRD patterns (Fig. 1a,b and Fig. S1, Supporting Information) and Rietveld refinements (Table S1 and S2, Supporting Information). Upon reduction at 800 °C in $H_2$, an additional reflection indexed to $Fm\bar{3}m$ (No. 221) appears, indicating decoration of the perovskite by *in situ* exsolved metallic nanoparticles. The double perovskite structure remains stable in both reducing and oxidizing atmospheres, which is crucial for the performance of electrode materials in S-SOFCs [61]. The high redox stability can be attributed to the strong chemical bonds formed between Mn and O ions [2]. A-site ordering in all compositions (reduced and oxidized) is confirmed by the (001) superlattice reflection at 11.5°, consistent with $SmBaMn_2O_{5+\delta}$ perovskites [5,18]. The diminished intensity of this peak in Fe-substituted samples (x = 0.45, 0.9) suggests partial Sm/Ba intermixing. The expected layered stacking [$LnO_\delta$ − $MnO_2$ − BaO − $MnO_2$ − $LnO_\delta$] along c is retained in the Fe-substituted compounds (Fig. 1c). Oxygen deficiency in the $LnO_\delta$ layers forms fast oxygen-ion diffusion channels, enhancing the ionic contribution to total conductivity [2,5,23,24]. The tetragonal cell of $\sqrt{2a_p} \times \sqrt{2a_p} \times 2a_p$ with tilted $MnO_6$ octahedra, ($a_p$: cubic perovskite primitive cell), is typical for A-site layered double perovskites [62]. At the B-site, Mn and Fe adopt rock-salt-like charge ordering: $Mn^{2+}/Mn^{3+}$ (and $Fe^{2+}/Fe^{3+}$ in Fe-substituted samples) dominate in reduced compounds, while $Mn^{3+}/Mn^{4+}$ (and $Fe^{3+}/Fe^{4+}$) prevail after oxidation [2,18,20,21]. A trace $BaMnO_3$-like hexagonal impurity (space group $P6_3/mmc$, No. 194) is detected in the oxidized Fe-free sample, consistent with prior reports for $Ln_{0.5}Ba_{0.5}MnO_{3+\delta}$ (Ln = Nd, Gd) [21,22]. No extraneous phases are observed in Fe-substituted materials (x = 0.45, 0.9), indicating Fe promotes structural stability.

Cation ordering during synthesis was analyzed using *ab initio* modeling through radial distribution functions (RDFs) of selected cation–cation pairs. Ensemble-averaged RDFs were generated under both Boltzmann and uniform weighting to distinguish thermodynamically favored configurations from random distributions. In the Boltzmann scheme, configurations were scaled by their Boltzmann factors to reflect thermally accessible states. As shown in Fig. 1d,e and Fig. S2 (Supporting Information), Boltzmann-weighted ensembles reveal distinct deviations from uniform weighting. For Mn—Mn pairs (Fig. 1d), the first peak is markedly reduced and the second peak is enhanced, indicating a lower probability of Mn—Mn nearest neighbors and a preference for second-shell association. A similar, though weaker, trend appears for Fe—Fe pairs (Fig. S2a, Supporting Information). Since Mn and Fe share the same B-site sublattice, these results indicate an energetic tendency toward alternating Mn/Fe arrangements (an established signature of B-site ordering in perovskites). For Mn—Ni and Mn—Co pairs (Fig. 1e and Fig. S2b, Supporting Information), the first peaks intensify under Boltzmann weighting, particularly for Mn—Ni, revealing a strong preference for Ni (and to a lesser extent Co) to occupy Mn nearest-neighbor positions. In contrast, Fe—Ni and Fe—Co pairs (Fig. S2c,d, Supporting Information) show reduced first peaks, suggesting that both dopants favor second-shell sites relative to Fe. Together, these correlations indicate that Ni and Co preferentially associate with Mn rather than Fe, reinforcing unlike-neighbor stabilization within the Mn/Fe sublattice. The effect is notably stronger for Ni. The reference $SmBaMnFeO_{5+\delta}$ shows nearly identical RDFs under both weighting schemes, confirming the absence of significant ordering in the undoped system. To probe the impact of Fe incorporation on lattice dynamics, element-projected vibrational densities of states (vDOS) were computed for x = 0, 0.45, and 0.9 (Fig. 1f). The Mn-projected vDOS exhibits a clear blue shift with increasing Fe content, indicating progressive hardening of Mn—O vibrational modes, whereas the Fe-projected vDOS remains nearly unchanged. This stiffening of Mn—O bonds correlates with the experimentally observed improvement in structural robustness upon Fe substitution. No evidence of static Jahn–Teller distortions was found, as neither diffraction nor local probes revealed the characteristic two-long/four-short Mn—O pattern. These findings demonstrate that Fe incorporation stabilizes the perovskite framework primarily by strengthening Mn—O interactions and suppressing lattice instabilities, rather than through Jahn–Teller-driven symmetry breaking.

Interestingly, no significant differences in structural properties were observed between nanofiber and powder $Sm_{0.9}Ba_{0.9}Mn_{1.8-x}Fe_xCo_{0.1}Ni_{0.1}O_{5+\delta}$ (x = 0, 0.45, 0.9) samples with identical chemical compositions (Fig. S3, Table S3 and S4, Supporting Information) [14]. However, due to their higher specific surface area and shorter diffusion lengths, nanofibrous samples enable single-phase double perovskite formation with *in situ* exsolved nanoparticles at lower temperatures, whereas powder samples require higher calcination temperatures to avoid secondary phase formation (Fig. S4, Supporting Information). The slightly larger unit-cell volumes in Fe-substituted samples (x = 0.45, 0.9) likely reflect differences in oxygen non-stoichiometry and the lower average Fe oxidation state compared to Mn. The weight fraction of the exsolved metallic phase was estimated at 4.73%, 6.46%, and 4.73%, for samples with x = 0, 0.45, and 0.9, respectively. For reduced samples, the diffraction segment 43.8–44.6° shifts to lower angles with increasing Fe content (Fig. 1g) suggesting the incorporation of Fe into the *in situ* exsolved Co—Ni alloy, since the atomic radius of Fe is larger than that of Co and Ni. This confirms that higher Fe substitution in the perovskite leads to greater Fe content in the metallic nanocatalysts. The strong intensity of the reflection from the (111) planes reveals that these crystals play a dominant role in the metallic nanoparticles, while the diffraction peaks at (220) and (200) are negligible, which was also observed for other Fe-based alloy nanoparticles [63].

Interestingly, after oxidation in air, the metal nanoparticles transform into $Co_3O_4$-type oxides (space group $Fd\bar{3}m$). The intensity of this additional spinel peak decreases with Fe content, suggesting partial re-dissolution of the exsolved phase in Fe-rich compositions (Fig. 1b and Fig. S1c,d, Supporting Information). The weight fraction of the spinel oxide phase was estimated at 4.61%, 4.01%, and 1.14%, for samples with x = 0, 0.45, and 0.9, respectively (Table S2, Supporting Information). Oxidized perovskites retain $P4/nmm$ symmetry but display reduced unit-cell parameters relative to the reduced state, reflecting the oxidation of Mn and Fe cations, vacancy annihilation, and compositional changes after exsolution. Such behavior is typical for electrode candidates for S-SOFCs [34]. The relative volume change between oxidized and reduced samples diminishes with Fe content (Fig. 1h). Notably, $Sm_{0.9}Ba_{0.9}Mn_{0.9}Fe_{0.9}Co_{0.1}Ni_{0.1}O_{5+\delta}$ exhibits the smallest $\Delta V$ (−3.08%), favorable for cycling between fuel and air atmospheres. The most Fe-rich target composition (x = 1.35) could not be obtained under the standard procedure (Fig. S5a, Supporting Information). Raising the calcination temperature to 1200 °C yielded a single-phase cubic perovskite ($Pm\bar{3}m$) (Fig. S5b, Supporting Information), but at the expense of nanofiber integrity. Moreover, this phase proved unstable

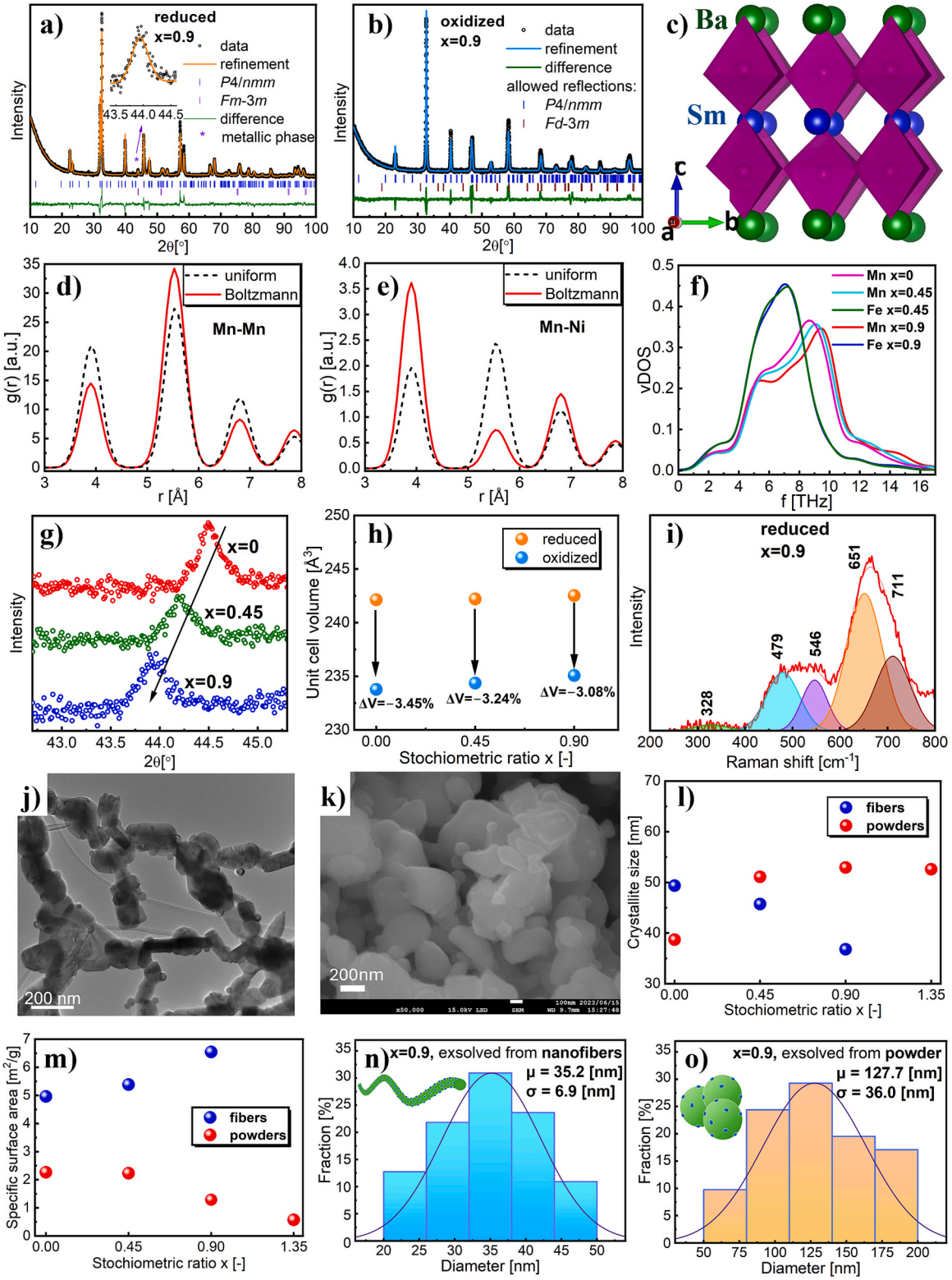


**Fig. 1.** XRD patterns with Rietveld refinement for $Sm_{0.9}Ba_{0.9}Mn_{0.9}Fe_{0.9}Co_{0.1}Ni_{0.1}O_{5+\delta}$ nanofibers: a) reduced in 5 vol% $H_2$/Ar at 900 °C and subsequently in $H_2$ at 800 °C for 2 h; and b) oxidized in air at 900 °C for 2 h; c) Crystal structure of the A-site-ordered $Sm_{0.9}Ba_{0.9}Mn_{1.8-x}Fe_xCo_{0.1}Ni_{0.1}O_{5+\delta}$ perovskite; Radial distribution functions for d) Mn—Mn and e) Mn—Ni pairs of $Sm_{0.9}Ba_{0.9}Mn_{0.9}Fe_{0.9}Co_{0.1}Ni_{0.1}O_{5+\delta}$; Results are presented using uniform and Boltzmann scaling; f) Partial vibrational density of states of Mn and Fe ions calculated for $Sm_{0.9}Ba_{0.9}Mn_{1.8-x}Fe_xCo_{0.1}Ni_{0.1}O_{5+\delta}$ (x = 0, 0.45, and 0.9) compositions; g) XRD pattern segment for $Sm_{0.9}Ba_{0.9}Mn_{1.8-x}Fe_xCo_{0.1}Ni_{0.1}O_{5+\delta}$ (x = 0, 0.45, and 0.9) samples; h) Unit cell volume of reduced and oxidized perovskites as a function of Fe-substitution level. Error values are smaller than the visible points; i) Raman spectra recorded for reduced $Sm_{0.9}Ba_{0.9}Mn_{0.9}Fe_{0.9}Co_{0.1}Ni_{0.1}O_{5+\delta}$ nanofibers. Micrographs of $Sm_{0.9}Ba_{0.9}Mn_{0.9}Fe_{0.9}Co_{0.1}Ni_{0.1}O_{5+\delta}$ j) nanofibers and k) powder samples; l) Average perovskite crystallite size calculated using Scherrer equation; m) Specific surface area determined by BET for $Sm_{0.9}Ba_{0.9}Mn_{1.8-x}Fe_xCo_{0.1}Ni_{0.1}O_{5+\delta}$ nanofiber and powder perovskites. Histograms of the diameter of exsolved nanoparticles from n) nanofibers, and o) powder $Sm_{0.9}Ba_{0.9}Mn_{0.9}Fe_{0.9}Co_{0.1}Ni_{0.1}O_{5+\delta}$ materials.

under fuel-electrode conditions and is unsuitable for symmetrical operation.

Although Raman spectroscopy does not probe the metallic exsolved phase, it is informative for the perovskite matrix and its distortions. Consistent with Hua et al. [64], who observed no Raman peaks for the reduced ordered $(PrBa_{0.85}Ca_{0.15})_{0.5}(MnFe)_{0.5}O_{3-\delta}$ (*P*4/*nmm*) and a broad 675 $cm^{-1}$ band in the oxidized state (oxygen motion in Mn(*Fe*)$O_6$ octahedra associated with Jahn-Teller distortion), the Raman spectra recorded for $Sm_{0.9}Ba_{0.9}Mn_{0.9}Fe_{0.9}Co_{0.1}Ni_{0.1}O_{5+\delta}$ nanofibers (Fig. 1i) show modes attributable to $MnO_x/FeO_x$ octahedra: 200–450 $cm^{-1}$ (skeletal), 450–550 $cm^{-1}$ (M–O–M deformation), and 550–750 $cm^{-1}$ (M–O stretching) [65]. For *P*4/nmm (No. 129) symmetry, there are 21 possible Raman-active modes: $6A_{1g} + 3B_{1g} + 2B_{2g} + 9E_g$ [66]. During *in situ* oxidation, the Raman spectrum exhibited only minor changes, suggesting a comparable degree of crystal structure distortion (Fig. S6, Supporting Information). At elevated temperatures, increased phonon motion within the structure results in poor quality of Raman spectra (Fig. S7, Supporting Information). Spectra collected at multiple locations (Fig. S8, Supporting Information) show identical band positions.

Morphologies shown in Fig. 1j and Fig. 1k demonstrate the benefits provided by the fabrication of nanofibers, such as promoting rapid gas diffusion, robust connectivity enabling continuous transport pathways, smaller grain size and a large number of reactive sites. Micrographs presented in Fig. S9 and S10 (Supporting Information) revealed that the $Sm_{0.9}Ba_{0.9}Mn_{1.8-x}Fe_xCo_{0.1}Ni_{0.1}O_{5+\delta}$ (x = 0 and 0.9) nanofibers are composed of large nanocrystals, in direct contact, assembling into fiber-like nanostructures. The fibers are interconnected, forming a network structure characterized by voids several hundred nanometers in size. The nanofiber diameters are irregular, ranging from 100 to 170 nm for the sample of x = 0, and from 70 to 140 nm for the perovskite of x = 0.9. The Fe-free nanofibers (x = 0) are composed of significantly larger grains compared to those of x = 0.9. Notably, the nanofiber morphology prior to calcination shows no differences (Fig. S11, Supporting Information), indicating that the electrospinning parameters were effectively optimized for all compositions. The differences in morphology appear only after the calcination process. This result suggests that Fe substitution in the $Sm_{0.9}Ba_{0.9}Mn_{1.8-x}Fe_xCo_{0.1}Ni_{0.1}O_{5+\delta}$ perovskite structure suppresses grain growth and sintering kinetics. For SOFCs, this is highly beneficial, as it may enable long-term operational stability and preserve the favorable microstructure in terms of continuous porosity, high specific surface area, and an increased number of catalytically active sites [29,45]. Micrographs of powder samples presented in Fig. S12 (Supporting Information) show the presence of both small particles (~300 nm) and a certain degree of agglomeration from the nanometric to micrometric range. The SEM observations confirm the polycrystalline nature of the samples, with a random shape and distribution of grains. Some powders appear to contain quasi-spherical particles.

The mean crystallite size of nanofibers and powders calculated by the Scherrer equation is shown in Fig. 1l. This equation provides an estimated value of the size of the X-ray diffracted crystalline domains. This method neglects contributions from lattice strain; however, the maximum strain in crystallites is expected for the sample of x = 0.9, where the concentrations of Fe and Mn ions are equal. An equimolar ratio of transition metal cations may induce inhomogeneity in the B-site sublattice, leading to lattice distortion due to the mismatch in ionic radii between Fe and Mn ions. Elevated lattice strain is also associated with a higher concentration of structural defects, such as oxygen vacancies [67].

For nanofibers calcined for 2 h at 900 °C in air and subsequently reduced at 900 °C in 5 vol% $H_2$/Ar and at 800 °C in $H_2$, increasing Fe substitution leads to a decrease in average crystallite size, consistent with the morphology observed by high-resolution TEM. Nanofibers without Fe substitution exhibit larger diameters and locally coalesced grains, indicating enhanced grain growth. Higher Fe content in nanofibers may promote Fe segregation to grain boundaries and slow the sintering kinetics, which would yield smaller crystallites and higher specific surface area, consistent with Fe-segregation behavior reported for Fe-doped $SrTiO_3$ [68]. Importantly, the specific surface area trend determined by BET (Fig. 1m) follows the Scherrer-derived crystallite-size trend for nanofibers. As the average crystallite size decreases with Fe incorporation, the specific surface area of $Sm_{0.9}Ba_{0.9}Mn_{1.8-x}Fe_xCo_{0.1}Ni_{0.1}O_{5+\delta}$ nanofibers increases from 4.96 $m^2$ $g^{-1}$ (x = 0) to 6.54 $m^2$ $g^{-1}$ (x = 0.9).

In contrast, powder samples with x = 0–1.35, calcined for 10 h at 1000 °C in air and subsequently reduced at 950 °C in 5 vol% $H_2$/Ar and at 800 °C in $H_2$, show an opposite trend. Upon introducing Fe at a concentration level of x = 0.45 on the Mn site, the crystallite size increased sharply from 38.7 nm to 51.1 nm and continued to increase slightly with further Fe incorporation, reaching 52.6 nm at x = 1.35. Notably, the x = 1.35 sample, calcined at 1200 °C without a reduction treatment, does not exhibit a stepwise increase in crystallite size, which may be attributed to the retention of transition metal cations in higher oxidation states within the perovskite lattice. Overall, these results indicate that powder crystallinity increases with Fe content, likely related to unit-cell expansion arising from the slightly larger ionic radius of $Fe^{3+}$ compared to $Mn^{3+}$ [67,69], whereas this effect is less pronounced in the nanofibers, for which Fe-driven suppression of crystallite coarsening dominates [68]. Similar trends have been reported for $La_{0.8}Ca_{0.15}Na_{0.05}Mn_{1-x}Fe_xO_3$ and $LaMn_{1-x}Fe_xO_3$ systems [67,69]. The specific surface area (Fig. 1m) decreases from 2.27 to 0.57 $m^2$ $g^{-1}$ for powders with x = 0 and x = 1.35, respectively. This monotonic decrease in BET specific surface area occurs concurrently with the increase in Scherrer-derived crystallite size, which is consistent with progressive crystallite coarsening. Notably, the x = 0.9 nanofibers exhibit approximately five times higher specific surface area than the corresponding powder.

Nanofibers also promote the formation of smaller exsolved nanoparticles than powders. The average diameter of nanoparticles exsolved from fibers was calculated as 39.3 nm and 35.2 nm for samples of x = 0 and x = 0.9, respectively (see Fig. 1n and S13a, Supporting Information), whereas in powder samples, exsolved nanoparticle diameters reached 80.2 nm and 127.7 nm for x = 0 and x = 0.9, respectively (see Fig. 1o and S13b, Supporting Information). The size difference arises from different coarsening rates and the finer-grained morphology of the nanofibers relative to the powders. For the x = 0.9 composition, the surface density of exsolved nanoparticles was estimated to be 105.5 $\mu m^{-2}$ for nanofibers, which is up to 20 times higher than for the corresponding powder (5.6 $\mu m^{-2}$). For the Fe-free composition (x = 0), densities are 4.9 $\mu m^{-2}$ (powders) and 23.5 $\mu m^{-2}$ (nanofibers).

Overall, nanofiber fabrication enhances exsolution by yielding smaller, more uniformly distributed nanoparticles and markedly improved electrocatalytic activity. We attribute this to (i) a high density of surface defects (oxygen vacancies, grain boundaries, dislocations) that act as preferential nucleation sites and lower the thermodynamic barrier; (ii) 1D morphology that facilitates mass transport and strain accommodation; and (iii) kinetic stabilization of nanoparticles at dislocations and other imperfections, which suppresses coarsening and maintains nanoscale dimensions over long operation [70]. Lower synthesis temperatures and shorter processing further favor smaller particles and are energy-efficient. Consistent with classical nucleation theory [38,39], higher exsolution temperatures reduce particle number density and increase size, a trend widely reported [39]. Because both morphologies contain identical concentrations of exsolvable cations, conservation of mass dictates that samples bearing smaller-diameter particles display higher number densities, exactly as observed.

### 2.2. *In situ* exsolution of metallic nanoparticles by reduction

A schematic comparison of the *in situ* exsolution process occurring in nanofibrous and powder perovskites is illustrated in Fig. 2a. Microscopy reveals that the exsolved nanoparticles are quasi-spherical and partially embedded ("socketed") in the host oxide (Fig. 2b and Fig. S14,

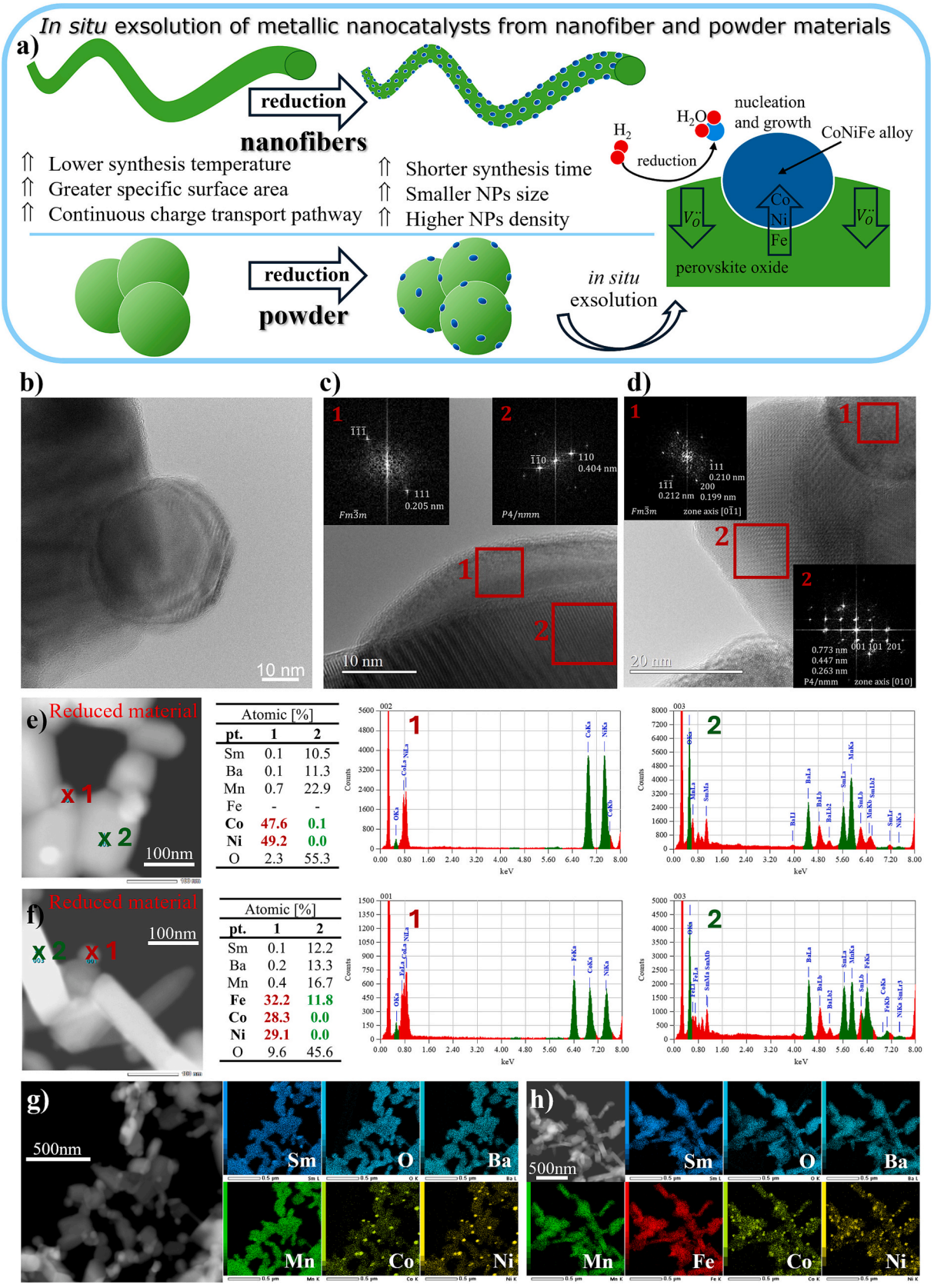


**Fig. 2.** a) Schematic comparison of the *in situ* exsolution process in nanofibers and powder perovskites; b) HR-TEM image of the nanoparticle exsolved from $Sm_{0.9}Ba_{0.9}Mn_{0.9}Fe_{0.9}Co_{0.1}Ni_{0.1}O_{5+\delta}$ nanofibers reduced in pure hydrogen; HR-TEM with the Fast Fourier Transform (FFT) analysis of reduced c) $Sm_{0.9}Ba_{0.9}Mn_{1.8}Co_{0.1}Ni_{0.1}O_{5+\delta}$ and d) $Sm_{0.9}Ba_{0.9}Mn_{0.9}Fe_{0.9}Co_{0.1}Ni_{0.1}O_{5+\delta}$ compounds; The point EDX analysis of reduced e) $Sm_{0.9}Ba_{0.9}Mn_{1.8}Co_{0.1}Ni_{0.1}O_{5+\delta}$ and f) $Sm_{0.9}Ba_{0.9}Mn_{0.9}Fe_{0.9}Co_{0.1}Ni_{0.1}O_{5+\delta}$ nanofibers, along with EDX spectra measured at the indicated points; The EDX map of element distribution for the reduced g) $Sm_{0.9}Ba_{0.9}Mn_{1.8}Co_{0.1}Ni_{0.1}O_{5+\delta}$ and h) $Sm_{0.9}Ba_{0.9}Mn_{0.9}Fe_{0.9}Co_{0.1}Ni_{0.1}O_{5+\delta}$ materials.

Supporting Information), consistent with prior reports [15,29,31,37,71,72]. The migration of a socketed nanoparticle on the surface requires diffusion both within the nanoparticle itself and along the leading edge of the supporting perovskite oxide. This anchoring mechanism therefore enhances resistance to particle coarsening, which is a common degradation pathway and a major challenge in nanocatalysts prepared by infiltration or deposition [43]. Such anchoring also improves carbon-tolerance in hydrocarbon-fueled SOFCs, particularly for Ni-based nanocatalysts [29,37,38]. HR-TEM studies with Fast Fourier Transform (FFT) analysis (Fig. 2c,d) confirm perovskite $P4/nmm$ symmetry and a metallic nanophase with $Fm\bar{3}m$ symmetry, in agreement with the previous XRD analysis. For the sample of x = 0, the metallic interplanar spacing 2.05 Å is indexed to (111), and the perovskite spacing 4.04 Å corresponds to (110). For x = 0.9, metallic spacings of 2.10 Å, 1.99 Å, and 2.12 Å index to (111), (200), and ($1\bar{1}\bar{1}$), while perovskite spacings of 2.63 Å, 4.47 Å, and 7.73 Å index to (001), (101), and (201), respectively. Compositional analysis shows that Fe-free perovskites (x = 0) are decorated by Co—Ni nanoparticles, whereas Fe-substituted oxides (x = 0.9) host Co–Ni–Fe exsolved nanoparticles with approximately equal amounts of each metal, as found by EDX point measurement presented in Fig. 2e and f. Powder samples exhibit the same Co/Ni/Fe enrichment (Fig. S15, Supporting Information). Under reduction, nearly all Ni and Co are *in situ* exsolved to the surface as metallic nanocatalysts. Fig. 2g and h show the elemental distribution in reduced nanofibers.

From a thermodynamic perspective, among Co, Ni, and Fe, iron is the most difficult to reduce to the metallic state and *in situ* exsolve under fuel electrode conditions [33]. The *in situ* exsolution ability of Fe is highly influenced by cations at the A- and B-sites in the perovskite, as well as by surface modification [16]. In some systems Fe does not exsolve (*e.g.* $PrBaMn_{1.7}Fe_{0.3}O_{5+\delta}$) [73], in others it exsolves only within specific dopant windows (*e.g.*, $Sr_2Fe_{2-x}W_xO_{6-\delta}$: Fe metal for x = 0.1–0.2, none for x = 1) [74], and in certain cases Fe exsolution is triggered by prior Cu exsolution, forming Janus nanostructures (*e.g.*, $La_{0.43}Sr_{0.37}Fe_{0.09}Cu_{0.03}Ti_{0.88}O_{3-\delta}$) [41].

In the present system of $Sm_{0.9}Ba_{0.9}Mn_{1.8-x}Fe_xCo_{0.1}Ni_{0.1}O_{5+\delta}$ perovskites, Co and Ni metals appear to be exsolved together from the sample of x = 0, forming homogeneous, round-shaped Co—Ni nanoparticles, while in the Fe-substituted compound with x = 0.9, Ni and Co are probably exsolved first, followed by Fe. It is believed that the exsolution process starts at relatively low temperatures. For instance, Ni exsolution from $La_{0.52}Sr_{0.28}Ti_{0.94}N_{i0.06}O_{3\pm d}$ perovskite begins at approximately 500 °C [39]. Under these conditions, ion mobility is weak, and the surface facilitates the nucleation of numerous nuclei with limited growth. As the temperature increases, enhanced ion mobility favors the diffusion of species capable of being *in situ* exsolved toward growing nuclei, promoting coarsening of the exsolved particles rather than the nucleation of additional nanocatalysts [38,39]. Furthermore, the elevated temperature increases the oxygen deficiency within the perovskite lattice. This promotes the exsolution kinetics because, during the diffusion of cations to the surface to form nanoparticles, oxygen vacancies move in the opposite direction [39,40].

Applying identical reduction protocols to powders and nanofibers can still yield larger nanoparticles in fibers than in powders. For example, Ni particles from $La_{0.52}Ca_{0.28}Ni_{0.06}Ti_{0.94}O_3$ averaged 15.9 nm (powders) *versus* 25.7 nm (nanofibers), attributed to lower surface energy and shorter cation diffusion paths in fibers; the exsolution rate was also faster in fibers under $H_2$ reduction [40]. Because coarsening drives catalyst deactivation, nanofibers decorated at lower temperature with smaller particles are attractive for long-term operation at high activity [43]. Interestingly, elemental segregation depends on Fe content and morphology. For x = 0, EDX studies reveal Mn/Ba segregation in powders (Fig. S16, Supporting Information) and Sm/Ba segregation in nanofibers (Fig. S17, Supporting Information). While introducing Fe (x = 0.45 and 0.9) suppresses segregation and enhances chemical stability, consistent with XRD studies for x = 0 sample, which shows additional peaks from $BaMnO_3$-like and $Sm_2O_3$-like impurities [21,22].

Thermal expansion behavior during the reduction of oxidized $Sm_{0.9}Ba_{0.9}Mn_{1.8-x}Fe_xCo_{0.1}Ni_{0.1}O_{5+\delta}$ (x = 0, 0.45, and 0.9) sinters, recorded by dilatometry in 5 vol% $H_2$/Ar flow, is presented in Fig. S18 (Supporting Information). Chemical expansion of all materials, resulting from changes in the oxidation state of transition metals, occurs between 300 °C and 500 °C. Materials are fully reduced in 5 vol% $H_2$/Ar during heating up to 500 °C, as similarly observed for $BaLnMn_2O_{6-\delta}$ perovskites (Ln = Pr, Nd, Sm, Gd, Dy, Er) [18].

The chemical reduction of the x = 0 oxide undergoes in two evident steps. The first step takes place between 300 °C and 390 °C and is associated with the reduction of $Mn^{4+}$ to $Mn^{3+}$. The second stage begins around 415 °C and ends at 500 °C, corresponding to the reduction of $Mn^{3+}$ to $Mn^{2+}$ [7,18]. An inflection on the reduction curves indicates the formation of the oxygen vacancy-ordered $SmBaMn_2O_{5.5}$-type structure [18]. For the x = 0.45 sample, the thermal-expansion response is dominated by the stepwise reduction of Mn ions, whereas x = 0.9 exhibits a single-step chemical reduction, suggesting that Mn- and Fe-related redox processes (and, to a lesser extent, those of Co and Ni) overlap and broaden, producing one merged chemical-expansion response. This is consistent with literature reports showing that reduction in hydrogen-containing atmosphere is commonly multistep, accompanied by significant lattice-oxygen release, and involves reduction of Mn, Fe, and Ni species [75,76]. Interestingly, a contraction is observed in the 770–900 °C range for the x = 0.9 sample. This behavior is most likely associated with Fe exsolution, since this trend was not observed for the oxide of x = 0. The magnitude of the contraction increases with increasing content of iron. A near-zero TEC within this temperature range was observed for the perovskite of x = 0.45.

### 2.3. *In situ oxidation of reduced materials*

The *in situ* oxidation process provides crucial insight into the behavior of exsolved nanoparticles under air electrode conditions, where metallic nanocatalysts may either re-dissolve into the perovskite lattice or reoxidize into nano-oxide phases. Upon heating in air, both the $Sm_{0.9}Ba_{0.9}Mn_{1.8-x}Fe_xCo_{0.1}Ni_{0.1}O_{5+\delta}$ (x = 0, 0.45, and 0.9) perovskite matrix and the exsolved metallic nanoparticles undergo oxidation. Depending on the chemical composition, the nanocatalysts can adopt a hollow core–shell structure (Fig. 3a).

For the oxidized Fe-free $Sm_{0.9}Ba_{0.9}Mn_{1.8}Co_{0.1}Ni_{0.1}O_{5+\delta}$ sample, the exsolved nanoparticles appear to be single-crystalline and homogeneous. As shown in Fig. S19a (Supporting Information), the nanoparticles exhibit a polyhedral shape with well-crystallized low-index faces, and this shape can be achieved when nanoparticles are anchored to the support. The shape of exsolved nanoparticles may determine their electrochemical properties and is influenced by many factors, such as synthesis conditions, grain size, and the socketing mechanism. The growth of exsolved particles may be epitaxial, meaning it is strongly dependent on the orientation of the support crystal [72]. Polyhedral nanoparticles possess a higher surface-to-volume ratio than spherical ones (a sphere retains ≈90% of a dodecahedron's surface area of equal volume). Consequently, polyhedral particles generally display enhanced catalytic activity. For instance, shape-evolved Ni nanocatalysts exsolved from $La_{0.75}Ca_{0.25}Ni_{0.25}Ti_{0.75}O_3$ exhibited superior and more stable activity under harsh hydrocarbon dry-reforming conditions than their spherical counterparts [72].

In Fe-rich perovskites (x = 0.9), the exsolved nanoparticles are polycrystalline, composed of multiple sintered crystallites (Fig. 3b). Their polycrystalline character likely arises from compositional heterogeneity. Oxidation of Fe–Co–Ni alloys can produce mixed oxides with the general formula $Fe_{3-x-y}Ni_xCo_yO_4$ [52]. Interestingly, a lighter contrast in the nanoparticle cores (Fig. 3b and Fig. S19b, Supporting Information) suggests the presence of a hollow interior. The formation of hollow core–shell $Fe_{3-x-y}Ni_xCo_yO_4$ spinel nanoparticles can be

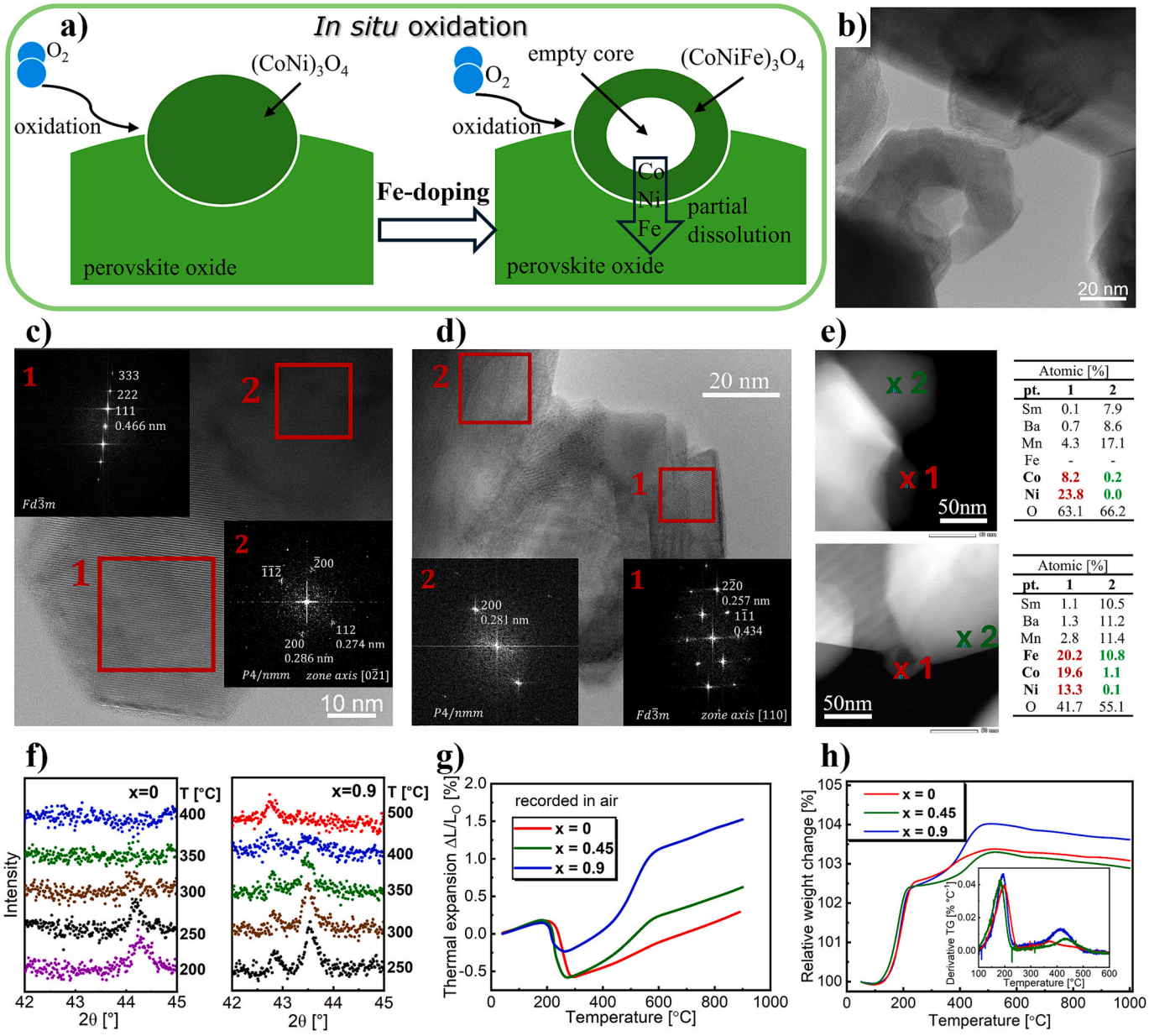


**Fig. 3.** a) Comparison of oxidation in Fe-free and Fe-substituted Mn-based perovskites with *in situ* exsolved nanoparticles. b) HR-TEM image of oxidized nanoparticle exsolved from $Sm_{0.9}Ba_{0.9}Mn_{0.9}Fe_{0.9}Co_{0.1}Ni_{0.1}O_{5+\delta}$ perovskite; HR-TEM with FFT analysis of oxidized c) $Sm_{0.9}Ba_{0.9}Mn_{1.8}Co_{0.1}Ni_{0.1}O_{5+\delta}$ and d) $Sm_{0.9}Ba_{0.9}Mn_{0.9}Fe_{0.9}Co_{0.1}Ni_{0.1}O_{5+\delta}$ compounds; e) The point EDX analysis of oxidized nanofibers $Sm_{0.9}Ba_{0.9}Mn_{1.8}Co_{0.1}Ni_{0.1}O_{5+\delta}$ (top illustration) and $Sm_{0.9}Ba_{0.9}Mn_{0.9}Fe_{0.9}Co_{0.1}Ni_{0.1}O_{5+\delta}$ (bottom illustration); f) Segment from HT-XRD pattern for $Sm_{0.9}Ba_{0.9}Mn_{1.8-x}Fe_xCo_{0.1}Ni_{0.1}O_{5+\delta}$ (x = 0 and 0.9); g) Thermal expansion behavior recorded during oxidation of reduced $Sm_{0.9}Ba_{0.9}Mn_{1.8-x}Fe_xCo_{0.1}Ni_{0.1}O_{5+\delta}$ (x = 0, 0.45, and 0.9) sinters by dilatometry in air; h) Oxygen content change of $Sm_{0.9}Ba_{0.9}Mn_{1.8-x}Fe_xCo_{0.1}Ni_{0.1}O_{5+\delta}$ recorded during heating for reduced compounds in air.

explained by a Kirkendall-type mechanism driven by strongly asymmetric cation diffusion during oxidation [53,54,77]. Kinetic studies have demonstrated that oxygen anion transport in $Fe_{3-x-y}Ni_xCo_yO_4$ spinel oxides is kinetically hindered (*e.g.* the activation energy for oxygen self-diffusion in $Co_3O_4$ is exceptionally high, reported as 736 kJ $mol^{-1}$ [54]), whereas cation diffusion can proceed much faster through octahedral–octahedral hopping pathways [53,54]. This imbalance in diffusion fluxes leads to vacancy accumulation in the nanoparticle core, resulting in void nucleation and the progressive development of hollow interiors [53,77]. Importantly, no hollow interior was observed for the corresponding Fe-free nanoparticles. This suggests that Fe incorporation modifies the oxidation and diffusion kinetics to favor sustained vacancy accumulation, thereby triggering void nucleation and the emergence of an empty core–shell morphology in the Fe-containing nanoparticles [53,77].

Concurrently, oxidation promotes partial re-dissolution of the exsolved Fe-containing metals into the perovskite lattice, while the remaining fraction forms a hollow core–shell structure. This partial reversibility is corroborated by XRD: with increasing Fe content, the intensity of reflections corresponding to Fe-containing spinel oxides diminish markedly upon oxidation. For x = 0.9, the reflection near 2θ = 36.5° becomes indistinguishable from the background (Fig. 1b and Fig. S1c,d, Supporting Information). Such hollow core–shell spinel nanocatalysts can enhance electrode functionality by shortening mass-transport pathways through the shell and increasing the density of electrochemically active sites, while the internal void provides mechanical "buffer space" that mitigates stress during redox cycling [53]. Moreover, the polycrystalline nature of these nanoparticles, composed

of numerous interconnected nanocrystallites, results in a high density of grain boundaries that act as catalytically active regions in electrochemical reactions [55]. To date, the literature typically describes solid core–shell systems, such as NiFe/$FeO_x$ nanoparticles exsolved from $Pr_{0.4}Sr_{1.6}(NiFe)_{1.5}Mo_{0.5}O_{6-\delta}$ double perovskite [31] or $Fe_{0.7}Ru_{0.3}$ alloy-$FeO_x$ exsolved from $(Pr_{0.5}Sr_{0.5})_{0.9}Fe_{0.8}Ru_{0.1}Nb_{0.1}O_{3-\delta}$ [30].

The FFT analysis of HR-TEM images (Fig. 3c and Fig. 3d) revealed well-oriented nanocrystals. Comparison with the simulated diffraction pattern along the same orientation confirmed that the oxidized nanoparticles for x = 0 and x = 0.9 adopt a $Co_3O_4$-type spinel structure, crystallizing in the cubic $Fd\bar{3}m$ space group [78]. Although HR-TEM cannot precisely resolve the multicomponent chemistry, the diffraction pattern combined with EDX (Fig. 3e) suggests $Co_3O_4$ or $NiCo_2O_4$ stoichiometry for x = 0. Due to nearly identical electron diffraction patterns of $NiCo_2O_4$ and $Co_3O_4$ [79], precise differentiation is challenging.

For x = 0.9, EDX indicates Fe, Co, and Ni-rich nanoparticles with complex stoichiometry, consistent with spinel-type phases of the general formula $Fe_{3-x-y}Ni_xCo_yO_4$ [52], such as $Fe_{0.5}Ni_{0.5}Co_2O_4$ [79] or $CoFe_2O_4$ [80]. No additional segregation was detected (Fig. S20). The lower Co and Ni signal intensities for x = 0.9 imply that Fe substitution promotes partial nanoparticle dissolution during oxidation. FFT spots from the perovskite support correspond to the $P4/nmm$ structure, confirming consistency with XRD observations, where the spinel reflections were too weak for reliable quantification.

High-temperature XRD (HT-XRD, Fig. 3f and Fig. S21, Supporting Information) identifies the oxidation onset: the metallic diffraction peak vanishes at 350 °C, 400 °C, and 500 °C for x = 0, 0.45, and 0.9 samples, respectively, signifying complete oxidation of the metallic phase. This temperature range is relatively low for Fe–Co–Ni oxidation but reflects nanoscale kinetics. Oxidation behavior depends strongly on particle size, shape, defect concentration, and synthesis conditions [52]. As particle dimensions decrease, diffusion paths shorten and oxidation accelerates. For instance, Ni nanoparticle oxidation begins near 300 °C, and activation energy drops from 54 kJ $mol^{-1}$ (400–700 °C) to 35 kJ $mol^{-1}$ (400–600 °C) as size decreases from 96 to 40 nm [81]. The theoretical oxidation tendency increases in the order Ni < Co < Fe, consistent with rising cation defect concentrations [82]. The reverse trend observed here (delayed oxidation in Fe-rich alloys) likely arises from the anchoring effect and multi-elemental entropy stabilization: as the number of metallic components increases, the entropic contribution to the Gibbs free energy enhances stability, lowering oxidation driving force at high temperature [83]. Upon oxidation, $Sm_{0.9}Ba_{0.9}Mn_{1.8-x}Fe_xCo_{0.1}Ni_{0.1}O_{5+\delta}$ (x = 0, 0.45, and 0.9) materials undergo a phase transition from $P4/nmm \rightarrow P4/mmm$ near 200 °C, evidenced by the disappearance of the (001) reflection at 11.5° (Fig. S22, Supporting Information) [5,18]. This transition accompanies rapid oxidation, causing a sharp unit-cell contraction typical for $LnBaMn_2O_{5+\delta}$ oxides [18]. Oxidation proceeds at lower temperatures than reduction because it is exothermic ($\Delta H = -218.3 \pm 35.1$ kJ $mol^{-1}$ for $BaYMn_2O_5$ [19]), providing local heating that facilitates oxygen diffusion. Morphology and synthesis conditions influence both oxidation kinetics and transition onset, though these parameters remain independent of Fe content in the present materials [14]. Consistently, dilatometry reveals material shrinkage during oxidation (Fig. 3g).

As shown in Fig. 3h, Fe substitution strongly affects oxidation behavior. Oxygen uptake data (Table S5, Supporting Information) show similar oxygen incorporation for x = 0 (3.38 wt%) and x = 0.45 (3.30 wt%), while x = 0.9 achieves higher uptake (4.02 wt%), exceeding that of $BaLnMn_2O_{6-\delta}$ (Ln = Pr, Nd, Sm, Gd, Dy, Er) [18]. The first Derivative Thermogravimetry (DTG) peak corresponds to perovskite oxidation, and the second to oxidation of exsolved nanoparticles, consistent with HT-XRD and dilatometry. The x = 0.9 perovskite shows the lowest oxidation temperature (506 °C) and the highest DTG rate (0.048% $°C^{-1}$), reflecting faster kinetics. The enhanced oxygen storage capacity of $Sm_{0.9}Ba_{0.9}Mn_{0.9}Fe_{0.9}Co_{0.1}Ni_{0.1}O_{5+\delta}$ correlates with its minimal volume change upon redox cycling (Fig. 1h) and the lowest chemical expansion observed in both reduction (Fig. S18, Supporting Information) and oxidation (Fig. 3g). Its superior oxidation kinetics likely originate from improved oxygen transport and the ability of exsolved nanoparticles to reversibly undergo oxidation/reduction without structural degradation. The resulting anchored, redox-active nanoparticles function as both oxygen storage centers and catalytic sites, highlighting their potential for redox cycling and chemical looping oxidation applications [1]. In Fe-substituted materials, Fe transitions between metallic and ionic states alongside Co and Ni, and the nanofibrous morphology further accelerates oxygen exchange while reducing activation temperature for these processes.

### 2.4. Thermomechanical and transport properties

In SOFCs, all functional components (including electrodes, electrolyte, interconnects, and sealing layers) must maintain mechanical and chemical compatibility during operation. Thus, beyond stability and electrochemical activity, thermomechanical compatibility is a key criterion for electrode materials. Matching thermal expansion coefficients (TECs) among components minimizes thermal stress, preventing cracking and delamination during thermal cycling and enabling long-term durability [84].

To examine the structural evolution of $Sm_{0.9}Ba_{0.9}Mn_{1.8-x}Fe_xCo_{0.1}Ni_{0.1}O_{5+\delta}$ (x = 0, 0.45, 0.9, and 1.35), HT-XRD measurements were performed in air from room temperature to 1000 °C. All samples remained single-phase throughout the studied range, exhibiting only slight peak shifts toward lower reflection angles with increasing temperature, consistent with lattice expansion (Fig. 4a and Fig. S23a,b, Supporting Information). A phase transition in $Sm_{0.9}Ba_{0.9}Mn_{1.8-x}Fe_xCo_{0.1}Ni_{0.1}O_{5+\delta}$ (x = 0, 0.45 and 0.9) perovskites from the $P4/nmm$ to the $P4/mmm$ space group, indicated by a weak diffraction peak at 11.5°, was detected at approximately 200 °C [5,18]. For $Sm_{0.9}Ba_{0.9}Mn_{1.8-x}Fe_xCo_{0.1}Ni_{0.1}O_{5+\delta}$ (x = 0, 0.45 and 0.9) perovskites, an anisotropic character of thermal expansion was observed, as shown in Fig. S23c (Supporting Information) and reported in previous research [14]. As can be seen in Fig. S24 (Supporting Information), the $Sm_{0.9}Ba_{0.9}Mn_{0.45}Fe_{1.35}Co_{0.1}Ni_{0.1}O_{5+\delta}$ sample shows a cubic $Pm\bar{3}m$ symmetry throughout the entire studied temperature range.

Dilatometry between 40 and 900 °C (Fig. 4b,c) further elucidates thermomechanical behavior. In air, a marked chemical expansion occurs above 700 °C, associated with oxygen vacancy formation. Under 5 vol% $H_2$/Ar, the samples show nearly linear expansion, implying a stable oxygen content during heating. TECs derived from Rietveld refinement and dilatometry (Table S6, Supporting Information) increase slightly with Fe content, consistent with enhanced lattice oxygen mobility. The TEC values remain comparable to those of common electrolytes, such as $Ce_{0.8}Gd_{0.2}O_{1.9}$ ($12.7 \times 10^{-6}$ $K^{-1}$), $La_{0.8}Sr_{0.2}Ga_{0.8}Mg_{0.2}O_{3-\delta}$ ($11.3 \times 10^{-6}$ $K^{-1}$), and 8 mol% yttria-stabilized zirconia ($10.9 \times 10^{-6}$ $K^{-1}$) [6,84], indicating good compatibility with typical SOFC architectures. Because TEC correlates with oxygen vacancy concentration, Fe substitution at the B-site can also influence ionic transport [85].

The effect of iron content on the density-related structural response of $Sm_{0.9}Ba_{0.9}Mn_{1.8-x}Fe_xCo_{0.1}Ni_{0.1}O_{5+\delta}$ was evaluated from energy–volume E(V) curves and thermal lattice expansion for selected substitution levels (x = 0, 0.45, and 0.9). Fig. 4d presents the computed E(V) curves with energies shifted so that the minimum of each curve is set to E = 0, and the data were fitted using the Birch–Murnaghan equation of state to extract equilibrium volumes and elastic parameters. The x = 0.45 and x = 0.9 compositions exhibit very similar E(V) profiles, whereas x = 0 shows a slightly larger equilibrium volume, approximately 1.2% higher than that of x = 0.45, indicating a modest lattice expansion in the Fe-free limit. Fig. 4e shows the temperature dependence of the lattice parameter, revealing nearly identical thermal

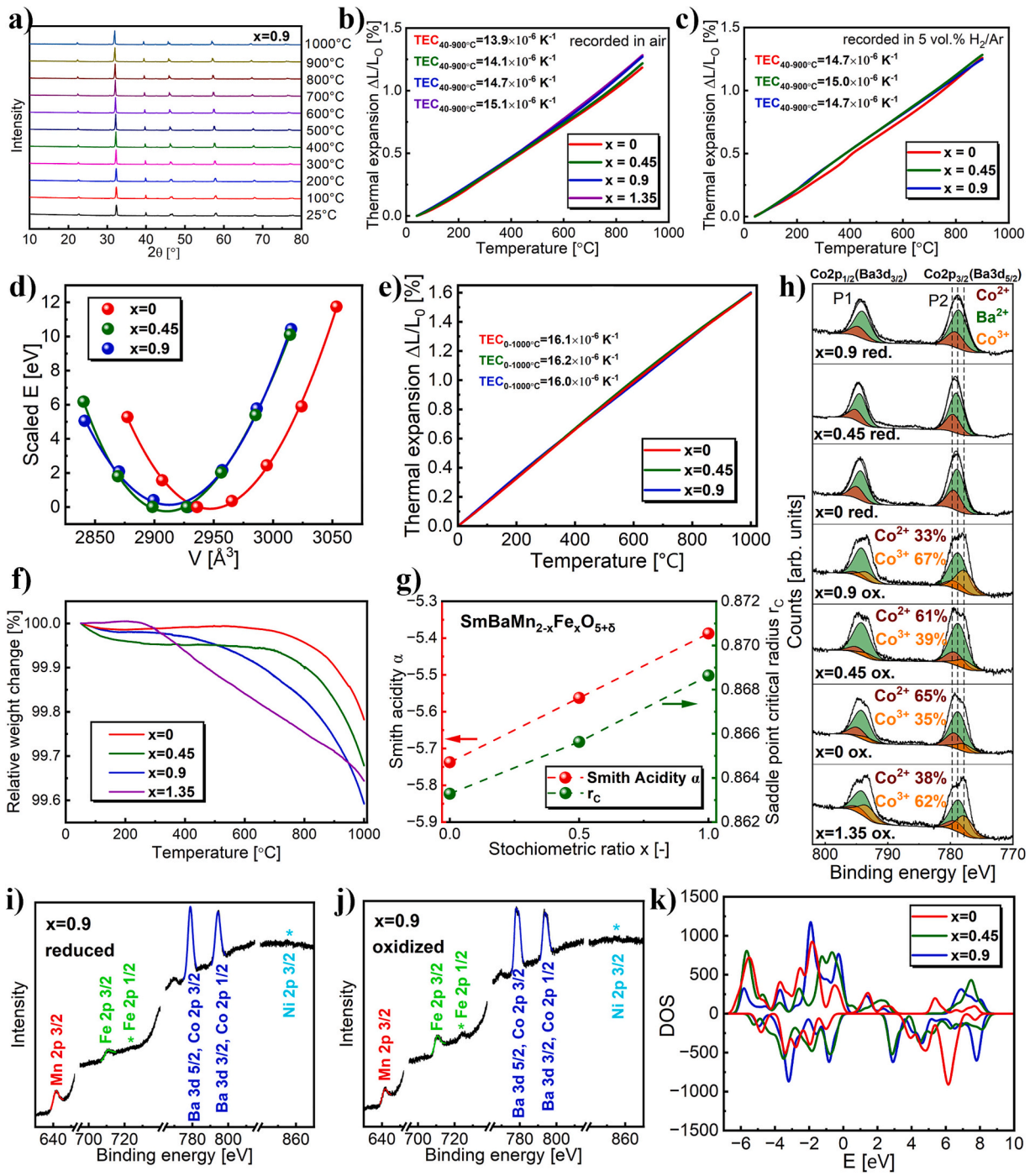


**Fig. 4.** a) HT-XRD pattern recorded in air on heating up to 1000 °C for oxidized $Sm_{0.9}Ba_{0.9}Mn_{0.9}Fe_{0.9}Co_{0.1}Ni_{0.1}O_{5+\delta}$; Thermal expansion behavior of $Sm_{0.9}Ba_{0.9}Mn_{1.8-x}Fe_xCo_{0.1}Ni_{0.1}O_{5+\delta}$ (x = 0, 0.45, 0.9, and 1.35) sinters by dilatometry measurements, recorded b) in air flow, and c) in 5 vol% $H_2$/Ar; d) E(V) curves calculated for $Sm_{0.9}Ba_{0.9}Mn_{1.8-x}Fe_xCo_{0.1}Ni_{0.1}O_{5+\delta}$ with their local minima shifted to E = 0; e) Theoretically calculated temperature evolution of lattice expansion coefficients for $Sm_{0.9}Ba_{0.9}Mn_{1.8-x}Fe_xCo_{0.1}Ni_{0.1}O_{5+\delta}$; f) Oxygen content change of $Sm_{0.9}Ba_{0.9}Mn_{1.8-x}Fe_xCo_{0.1}Ni_{0.1}O_{5+\delta}$ (x = 0, 0.45, 0.9, and 1.35), recorded during cooling in air; g) Smith acidity and saddle point critical radius of reduced $SmBaMn_{2-x}Fe_xO_{5+\delta}$ (x = 0, 0.45, and 0.9) perovskites; h) XPS spectra for $Sm_{0.9}Ba_{0.9}Mn_{1.8-x}Fe_xCo_{0.1}Ni_{0.1}O_{5+\delta}$ in Co 2p and Ba 3d regions; Wide XPS spectra for i) reduced and j) oxidized $Sm_{0.9}Ba_{0.9}Mn_{0.9}Fe_{0.9}Co_{0.1}Ni_{0.1}O_{5+\delta}$ samples; k) Spin-polarized density of states calculated for $Sm_{0.9}Ba_{0.9}Mn_{1.8-x}Fe_xCo_{0.1}Ni_{0.1}O_{5+\delta}$.

expansion among all three compositions, reaching an integrated linear expansion of about 1.6% at 1000 °C.

In perovskite oxides, efficient oxygen-ion conduction requires a high concentration of lattice vacancies and a low migration barrier (< 1 eV) [24]. Oxygen vacancy formation follows: $O_O^x \rightarrow V_O^{\bullet\bullet} + 2e^- + \frac{1}{2}O_2(g)$ [38]. Thermogravimetric (TG) analysis in air (Fig. 4f) reveals mass changes linked to oxygen release and uptake. For x = 0 and 0.45 samples, reduction begins above 700 °C, whereas Fe-rich samples (x = 0.9, 1.35) show onset at lower temperatures. This trend indicates that increasing Fe content lowers the activation energy for oxygen vacancy formation, promoting oxygen-ion transport within the SOFC operating window. The x = 1.35 composition, obtained by air calcination, exhibits a distinct TG profile due to differing redox behavior of $Fe^{4+}/Fe^{3+}$ and $Mn^{4+}/Mn^{3+}$ couples, with minimal influence from trace Co and Ni dopants.

Oxygen exchange kinetics can also be rationalized through the Smith acidity parameter ($\alpha$), which quantifies metal–oxygen bond strength and correlates inversely with oxygen exchange rate [86–88]. For double perovskites $AA'B_{2-x}B'_xO_6$: $\alpha_{AA'B_{2-x}B'_xO_6} = \frac{\alpha_{A'O}+\alpha_{AO}+(2-x)\alpha_{BO}+x\alpha_{B'O}}{4}$ [88]. The Smith acidity factor for reduced perovskite oxides was calculated assuming α values for $Sm_2O_3$, BaO, as well as FeO and MnO binary oxides relative to $H_2O$. For oxidized perovskites, $Fe_2O_3$ and $Mn_2O_3$ were considered [86,87].

Calculated $\alpha$ values (Fig. 4g and Fig. S25, Supporting Information) increase with Fe substitution in both reduced and oxidized $SmBaMn_{2-x}Fe_xO_{5+\delta}$, implying slightly slower surface exchange kinetics due to stronger Fe—O bonds. Another descriptor of ionic transport is the saddle-point critical radius ($r_c$), the geometric opening through which oxygen ions migrate, approximated as $r_c = \frac{-r_A^2+\frac{3}{4}a^2-\sqrt{2}a\times r_B+r_B^2}{2r_A+\sqrt{2}a-2r_B}$ [89], where $r_A$ and $r_B$ are ionic radii of A- and B-site cations, and $a$ is the pseudocubic lattice parameter. In most perovskite structures, $r_C$ generally does not exceed 1.0 Å, which is significantly smaller than the radius of the oxygen ion (1.40 Å). As a result, significant energy is required for oxygen transport through the saddle point, resulting in a high activation energy for oxygen-ion migration within the perovskite structure [89]. Iron substitution in reduced $SmBaMn_{2-x}Fe_xO_{5+\delta}$ (x = 0, 0.45, and 0.9) perovskites increases the saddle point critical radius $r_C$, favoring oxygen-ion transport in perovskites. In oxidized compounds, the trend is not straightforward. In redox-stable oxides, iron substitution causes a slight decrease in the $r_C$ value; however, the perovskite with the highest iron content (x = 1.35) exhibits the largest $r_C$ value (Fig. 4g and Fig. S25, Supporting Information).

The collected electrical conductivity data of $Sm_{0.9}Ba_{0.9}Mn_{1.8-x}Fe_xCo_{0.1}Ni_{0.1}O_{5+\delta}$ (x = 0, 0.45 and 0.9) oxides between 150 and 850 °C in 5 vol% $H_2$ atmosphere show that Fe substitution decreases total electrical conductivity in a reducing atmosphere (Fig. S26a, Supporting Information). The highest conductivity was recorded for the x = 0 (1.23 S $cm^{-1}$) sample at 850 °C, which is more than four times higher than that of the x = 0.9 (0.30 S $cm^{-1}$) and x = 0.45 (0.40 S $cm^{-1}$) samples at the same temperature. No straightforward correlation between iron content and electrical conductivity was observed in air (Fig. S26b, Supporting Information). The recorded conductivity at 850 °C in air was 2.54, 3.78, 1.51, and 4.89 S $cm^{-1}$ for the samples with x = 0, 0.45, 0.9, and 1.35, respectively. The highest value, 6.02 S $cm^{-1}$, was obtained for x = 0.45 material at 700 °C. Activation energies and extrapolated conductivities are summarized in Table S7 (Supporting Information).

X-ray photoelectron spectroscopy (XPS) analyses of reduced and oxidized samples (Fig. 4i,j, Fig. S27, Supporting Information) show a general shift toward lower binding energies after reduction, reflecting decreased oxidation states [90]. In the region presented in Fig. 4h, the Ba $3d_{5/2}$ and Co $2p_{3/2}$ peaks overlap around 780 eV, while Co $2p_{1/2}$ and Ba $3d_{3/2}$ peaks overlap around 796 eV, making interpretation challenging [9,91]. Nevertheless, Co is clearly reduced in $H_2$ relative to oxidized samples. Although quantitative assignment is challenging due to the dominant $Ba^{2+}$ signal and low Co/Ni contents, HR-TEM and FFT analyses confirm that exsolved Co–Ni–Fe nanoparticles are metallic after reduction, possibly coated with an ultrathin Co-oxide shell formed upon air exposure. Increasing Fe content enhances the proportion of $Co^{3+}$ species in oxidized samples, consistent with Fe participation in the exsolution/oxidation process. Mn and Fe exhibit mixed valence states at the material surface, dominated by $Mn^{2+}/Mn^{4+}$ and $Fe^{2+}/Fe^{3+}$ species in both reduced and oxidized samples, as reflected by the broad 2p features (Fig. S28a,b, Supporting Information), in agreement with previous reports on Mn-based perovskites [6,21]. The Ni 2p signal is indistinct due to its low concentration (Fig. S28c, Supporting Information). As XPS probes only the near-surface region, these oxidation states may differ from those in the bulk.

The electronic structure of $Sm_{0.9}Ba_{0.9}Mn_{1.8-x}Fe_xCo_{0.1}Ni_{0.1}O_{5+\delta}$ was examined through spin-polarized density of states (DOS) calculations, as shown in Fig. 4k. All investigated compositions display a pronounced asymmetry between spin-up and spin-down states, characteristic of magnetic materials. Partial saturation of the band gap is observed in each case, with the in-gap states predominantly spin-up and the lowest unoccupied molecular orbital (LUMO) states primarily spin-down. Notably, Fe incorporation mainly influences the spin-down LUMO states, shifting them to lower energies by approximately 1 eV compared to the Fe-free composition. In contrast, the x = 0 and x = 0.9 samples exhibit similar DOS profiles within the band gap region. The introduction of Fe induces partially filled d-states that undergo exchange splitting, displacing the spin-up and spin-down manifolds relative to one another and introducing states near the Fermi level. This progression transforms the initially less-conductive host into a spin-polarized conductor with increasing Fe concentration.

### 2.5. Rational electrode design: compatibility, kinetics, and power performance

A critical design parameter for SOFCs is the chemical stability of the electrolyte/electrode interface [92]. XRD diffractograms of 1:1 (mass) mixtures annealed at 800 °C for 100 h (comprising each electrolyte and the selected electrode materials) are shown in Fig. 5a and Fig. S29 (Supporting Information) for redox-stable compounds, and in Fig. S30 (Supporting Information) for the most Fe-rich composition (x = 1.35). Unit cell parameters and Rietveld results are summarized in Table S8–S12 (Supporting Information). In reduced mixtures, the 44–45° reflections arise from the *in situ* exsolved metallic phase. With GDC20, all materials are compatible in air. After heating in 5 vol% $H_2$, however, additional peaks at 35.1°, 41° (overlapping doublet), 51°, and 67.4° appear for x = 0 and 0.45, attributable to Gd-doped $BaCeO_3$ [93]. The intensity of these reflections decreases with Fe content; for x = 0.9, they are near background, indicating improved compatibility with GDC20 under reducing conditions. Thus, Fe substitution stabilizes the double perovskites at the GDC20 interface. In contact with LSGM, the materials are largely stable in both oxidizing and reducing atmospheres. Minor reflections observed at ~29.8° correspond to the (211) planes of $LnAGa_3O_7$-type oxides (Ln = La, Sm; A = Ba, Sr), which crystallize in the $P\bar{4}21m$ tetragonal crystal system [94]. Unfortunately, this phase has been identified as an electrical insulator that acts as a barrier to charge transport at the electrode/LSGM interface [95]. Because these impurities are negligible, LSGM was used directly (without buffer) in electrolyte-supported symmetrical cells. In contrast, the compounds react unfavorably with 8YSZ, forming $BaZrO_3$, $SmFeO_3$, and unidentified phases [3], necessitating a GDC20 barrier layer for the anode-supported 8YSZ cell. Overall reactivity with electrolytes is higher in reducing atmospheres, consistent with the stronger reflections from reaction products after reduction.

Symmetrical cells based on the LSGM electrolyte and $Sm_{0.9}Ba_{0.9}Mn_{1.8-x}Fe_xCo_{0.1}Ni_{0.1}O_{5+\delta}$ (x = 0, 0.45, and 0.9) nanofiber electrode materials were fabricated (see Experimental Section). Impedance studies in air show the lowest cathodic polarization resistance ($R_p$) for the composite cathode $Sm_{0.9}Ba_{0.9}Mn_{0.9}Fe_{0.9}Co_{0.1}Ni_{0.1}O_{5+\delta}$ + 30%GDC20 (Mn09-30GDC) with $R_p$ = 0.046, 0.074, 0.134 Ω $cm^2$ at 800, 750, 700 °C, respectively. The corresponding powder electrode shows substantially higher polarization resistance under identical conditions (Table S13, Supporting Information). Activation energies are 1.15 eV for the x = 0.45 and x = 0.9 nanofiber electrodes, indicating efficient ORR reactions under low-temperature SOFC conditions [96]. While the Fe-free (x = 0) material shows $E_a$ = 1.40 eV, indicating the lowest suitability as a low-temperature SOFC electrode. Notably, the obtained Rp values recorded in air are significantly lower than Mn- and/or Fe-based electrode materials reported for symmetrical SOFCs (Table S14, Supporting Information) [2,3,5–7,15].

Fig. 5b,c show Nyquist plots and DRT analyses. At lower temperatures, two peaks (P1, P2) are resolved: P1 shifts to higher frequency with

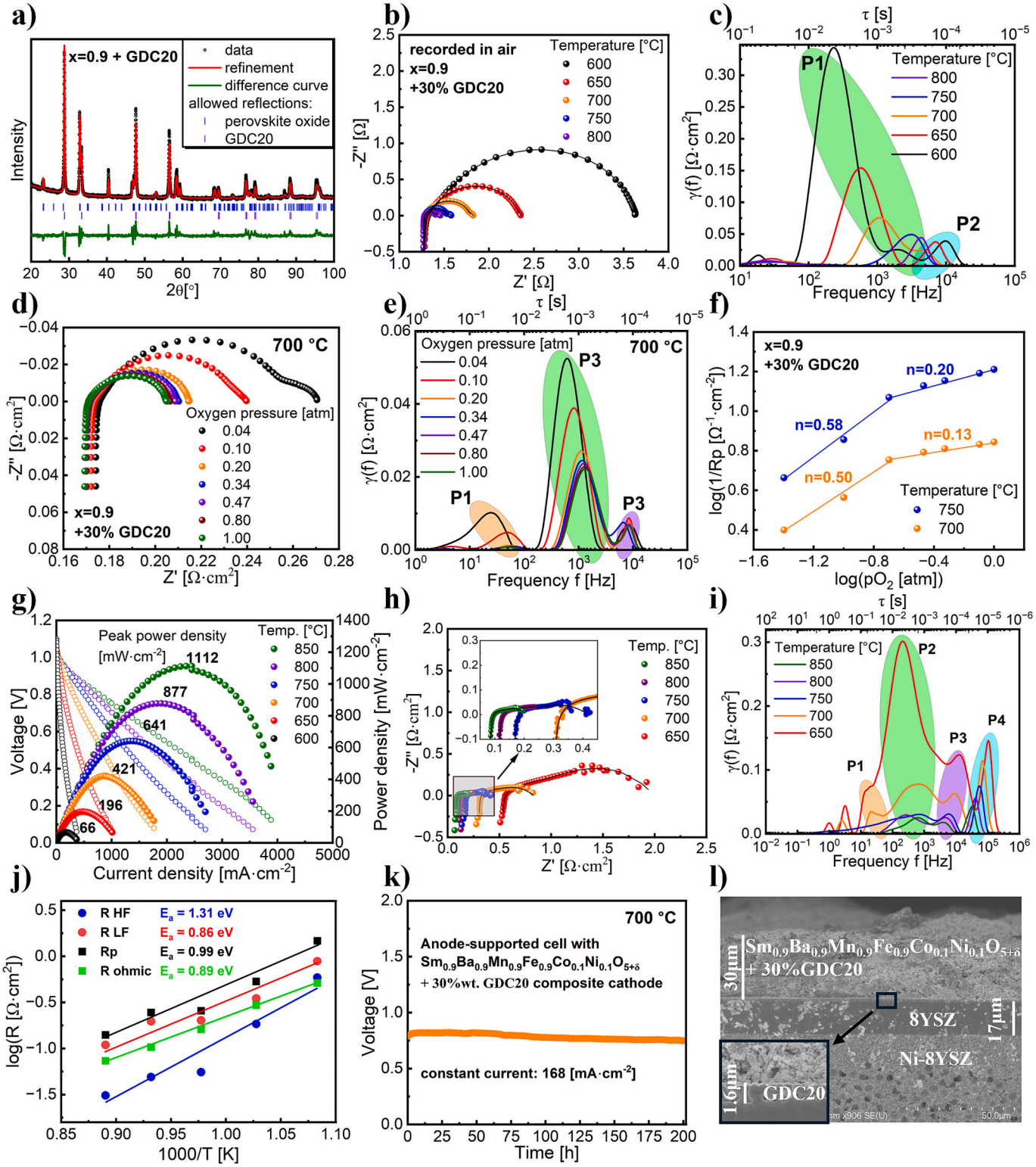


**Fig. 5.** a) XRD pattern of the 50:50 wt% $Sm_{0.9}Ba_{0.9}Mn_{0.9}Fe_{0.9}Co_{0.1}Ni_{0.1}O_{5+\delta}$ – GDC20 mixture annealed in air at 800 °C for 100 h; b) Nyquist plots and c) corresponding DRT profiles of the symmetrical cell with the best-chosen Mn09-30GDC composite electrode recorded in air; d) Nyquist plots and e) corresponding DRT profiles of the symmetrical cell with Mn09-30GDC composite electrode, recorded at 700 °C. $pO_2$ varies from 4% to 100% using Ar as carrier gas; f) Dependence of the Rp on the oxygen partial pressure at 700 °C and 750 °C recorded for the cell with Mn09-30GDC composite electrode; g) Voltage and power density as a function of the current density of $Sm_{0.9}Ba_{0.9}Mn_{0.9}Fe_{0.9}Co_{0.1}Ni_{0.1}O_{5+\delta}$ + 30%GDC20|GDC20|8YSZ|Ni + 8YSZ anode-supported cell with Ag current collector, along with h) Nyquist plots of the cell under open-circuit voltage conditions and i) DRT analysis of the corresponding EIS for the anode-supported cell; j) Temperature dependence of ohmic resistance $R_{ohmic}$, polarization electrode resistance Rp, along with $R_{HF}$ (high-frequency contribution) and $R_{LF}$ (low-frequency contribution) of anode-supported cell; k) Long-term stability test of anode-supported cell at 700 °C and constant current density of 168 mA $cm^{-2}$ (fuel cell mode); l) SEM micrograph of the anode-supported cross-section after testing.

temperature and is attributed to oxygen charge transfer, while P2 shifts to lower frequency and is associated with oxygen ions transport across the electrode–electrolyte interface [2]. Above 750 °C, the peaks merge into a single broad feature, indicating coupled polarization processes. Based on these results, the Mn09-30GDC composite was selected as the lead material for detailed cathode studies and preliminary S-SOFC evaluation.

Under varied oxygen partial pressure ($pO_2$), $R_p$ decreases monotonically with increasing $pO_2$ (Fig. 5d and S31a, Supporting Information): at 700 °C, $R_p = 0.399 \rightarrow 0.143\ \Omega\ cm^2$ for $pO_2 = 0.04 \rightarrow 1$ atm; at 750 °C, $R_p = 0.217 \rightarrow 0.062\ \Omega\ cm^2$. Spectra were fitted with a two-arc equivalent circuit (low- and high-frequency), with $R_p$ values summarized in Table S15 (Supporting Information). Because overlapping processes complicate assignment [44], DRT was used to deconvolute contributions (Fig. 5e and S31b, Supporting Information). Three peaks (P1–P3) are identified at 700–750 °C, with P2 dominant. P1 (low frequency) is most $pO_2$-sensitive and corresponds to $O_2$ dissociation; P2 is assigned to charge transfer (rate-limiting over broad $pO_2$); P3 (high frequency) shows weak $pO_2$ dependence and is linked to oxygen ions transport across the electrode–electrolyte interface [2]. The rate-limiting step was extracted using the power-law dependence $R_p = k \bullet p_{O_2}^{-n}$, with diagnostic n-values: $n = 1.0$ (gas diffusion/adsorption, $O_{2,\ gas} \rightarrow 2O_{2,\ ad}$), 0.5 (surface adsorption/dissociation, $O_{2,\ ad} \rightarrow 2O_{ad}$), 0.375/0.125 (two-step electron capture in charge transfer, $O_{ad} + e' \rightarrow O'_{ad}$ and $O'_{ad} + e' \rightarrow O''_{ad}$), 0.25 (overall charge transfer, $O_{ad} + 2e' + V_O^{\bullet\bullet} \rightarrow O_O^X$), 0 (bulk oxygen ions migration to electrolyte, $O^X_{O,\ cathode} \rightarrow O^X_{O,\ electrolyte}$) [2,8]. From the $\log(1/R_p)$–$\log(pO_2)$ plots (Fig. 5f), the low-$pO_2$ regime (0.04–0.20 atm) yields $n \approx 0.50$ (700 °C) and 0.58 (750 °C), indicating surface adsorption/dissociation as the primary limitation. At higher $pO_2$ (0.20–1.0 atm), charge transfer becomes rate-limiting (dominantly second-electron capture at 700 °C, first-electron capture at 750 °C). Because the cathode $pO_2$ during operation is below 1 atm, the operative limitation is expected to be oxygen surface adsorption and dissociation.

An anode-supported single cell with configuration $Sm_{0.9}Ba_{0.9}Mn_{0.9}Fe_{0.9}Co_{0.1}Ni_{0.1}O_{5+\delta}$ + 30%GDC20|GDC20|8YSZ|Ni + 8YSZ fueled by humidified $H_2$ achieved 1112, 877, 641, 421 mW $cm^{-2}$ at 850, 800, 750, 700 °C, respectively (Fig. 5g). These high-power densities underscore the benefit of nanofibers decorated with *in situ* exsolved polycrystalline hollow core–shell nanocatalysts. The corresponding Nyquist plots (Fig. 5h), together with DRT analysis (Fig. 5i) separate the operating-cell processes: negligible <5 Hz features at 650–700 °C (gas diffusion) vanish at higher temperature, indicating adequate electrode porosity. The low-frequency P1 ($10^1$–$10^2$ Hz) appears only under anode polarization; P2 ($10^2$–$10^3$ Hz) is dominant and attributed primarily to the cathode; P3 ($10^3$–$10^4$ Hz) corresponds to interfacial charge/ion transport; P4 (~$10^5$ Hz) reflects bulk electrolyte resistance [7]. Equivalent-circuit fits ($L\text{-}R_{ohm}\text{-}(RQ)_{HF}\text{-}(RQ)_{LF}$) show the low-frequency arc > high-frequency arc (Fig. 5j), indicating that performance is mainly limited by dissociative adsorption and/or surface diffusion process [74]. Across the measured temperature range, Rp remains higher than the ohmic resistance, consistent with polarization-limited performance (Table S16 and S17, Supporting Information). A 200-h stability test confirms the robustness of the Mn09-30GDC cathode (Fig. 5k). Post-mortem analysis shows a crack-free, well-adhered porous cathode tightly bonded to the electrolyte (Fig. 5l), consistent with matched TECs for the composite electrode, GDC20, and 8YSZ. The electrode maintains good porosity and sintered connectivity.

The I-V characteristic of the constructed symmetrical electrolyte-supported cell is shown in Fig. 6a, with the respective EIS

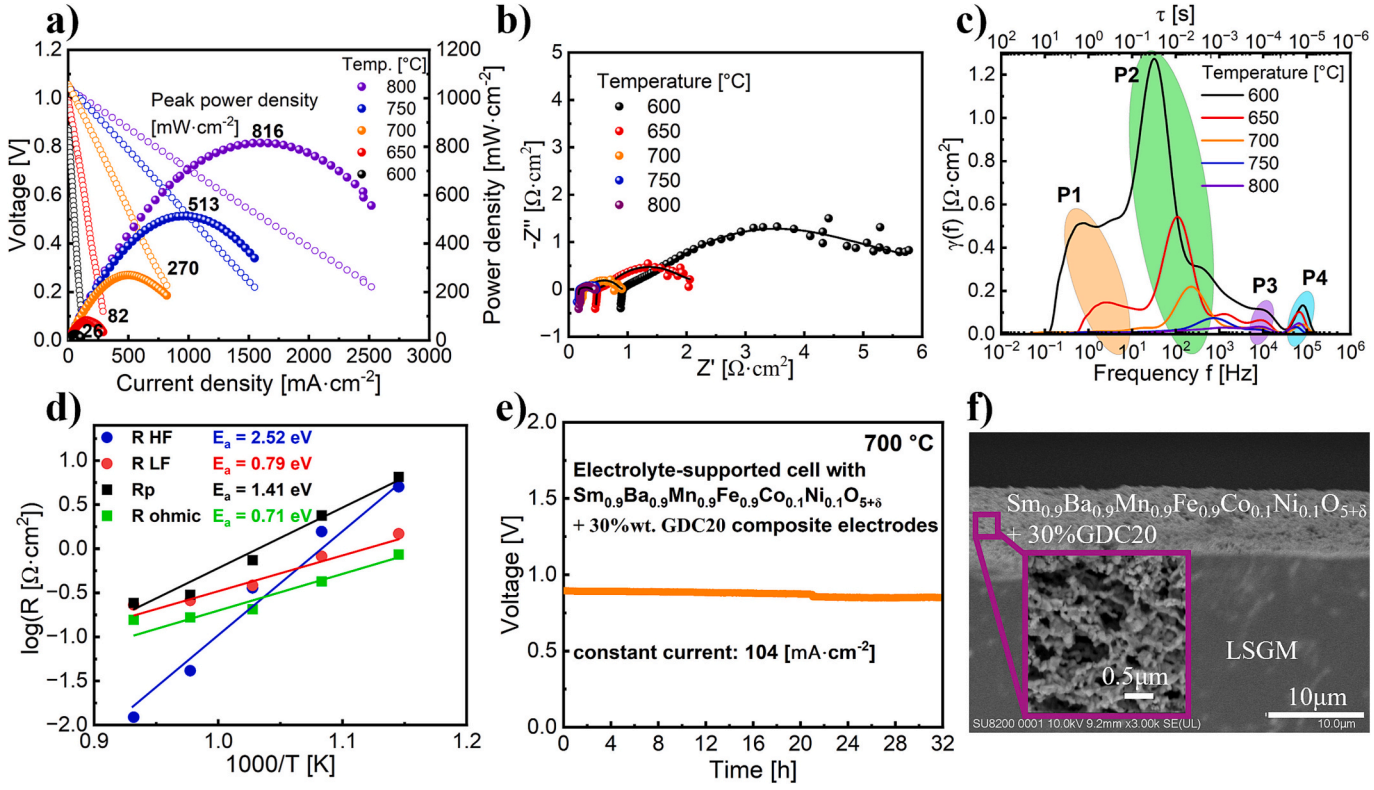


**Fig. 6.** a) Voltage and power density as a function of the current density of the symmetrical $Sm_{0.9}Ba_{0.9}Mn_{0.9}Fe_{0.9}Co_{0.1}Ni_{0.1}O_{5+\delta}$ + 30%GDC20|LSGM|$Sm_{0.9}Ba_{0.9}Mn_{1.8-x}Fe_xCo_{0.1}Ni_{0.1}O_{5+\delta}$ + 30%GDC20 electrolyte-supported cell with Ag current collector, along with b) Nyquist plots of the cell under open-circuit voltage conditions and c) DRT analysis of the corresponding EIS for the symmetrical electrolyte-supported cell; d) Temperature dependence of ohmic resistance $R_{ohmic}$, polarization electrode resistance Rp, along with $R_{HF}$ (high-frequency contribution) and $R_{LF}$ (low-frequency contribution) of the symmetrical electrolyte-supported cell; e) Short-term stability test of the symmetrical electrolyte-supported cell at 700 °C and constant current density of 104 mA $cm^{-2}$ (fuel cell mode); f) SEM micrograph of the symmetrical electrolyte-supported cross-section after testing.

characteristic in Fig. 6b. The nearly linear I − V curves, recorded for both anode-supported and electrolyte-supported cells, even at high current densities, suggest that nanofibrous electrodes have adequate porosity, minimizing negative concentration polarization effects. The symmetrical electrolyte-supported cell, powered by wet hydrogen, reached 816, 513, and 270 mW $cm^{-2}$ at 800, 750, and 700 °C, respectively. The obtained power densities significantly exceed those reported in the literature for S-SOFCs with Mn-based electrode materials (Table 1). The reported maximum power densities in previous studies were in the range of 296 - 481 mW $cm^{-2}$ at 800 °C, whereas the composite Mn09-30GDC electrodes proposed in this work achieve power densities from 70% to 176% higher compared to these literature values [2,5–7]. The excellent behavior arises from the integrated design: electrospun nanofiber morphology, *in situ* exsolution (Co–Ni–Fe metal on fuel electrode; $Co_3O_4$-type spinels/hollow core–shell oxides on air electrode), and optimized electrolyte fraction in the composite. Literature indicates Co–Ni–Fe metals promote $H_2$ dissociation, while $Co_3O_4$-type nano-oxides enhance charge transfer during ORR [2], consistent with the observed low $R_p$ (Table S16, Supporting Information).

The DRT profiles derived from the EIS spectra (Fig. 6c) reveal four characteristic peaks. The P1 peak ($10^0$–$10^1$ Hz) is most likely associated with the anode and disappears above 700 °C. The broad P2 peak ($10^1$–$10^3$ Hz) probably results from overlapping anodic and cathodic polarizations, whereas P3 (~$10^4$ Hz) and P4 (~$10^5$ Hz), similar to the anode-supported cell, are likely related to charge and ionic transport at the electrode/electrolyte interface and to the bulk electrolyte resistance, respectively [7]. Interestingly, the low-frequency arc is larger than the high-frequency arc (Fig. 6d) in the range at 700–800 °C, suggesting that the electrode efficiency is mainly limited by dissociative adsorption and/or surface diffusion phenomena [74]. At lower temperatures (600–650 °C), the polarization losses are dominated by the high-frequency arc, which is typical for SOFC anodes processes and can be attributed to hydrogen adsorption including charge transfer [97]. The high-frequency arc may also be attributed to oxygen ions transport across electrode/electrolyte interfaces and poor contact between the electrode and electrolyte particles in the composite (lack of percolation) [98]. As in the anode-supported cell, the Rp is higher across the entire temperature range than the ohmic resistance (Table S16 and S17, Supporting Information). Unfortunately, measurements in 5% $H_2$/Ar of symmetrical cells with LSGM and GDC20 electrolytes did not enable a clear separation of anodic and cathodic losses. For LSGM, the incomplete arc results from insufficient hydrogen concentration, while in GDC20, the Warburg-type response is attributed to its electronic conductivity (Fig. S32). Impedance measurements in pure hydrogen were not feasible due to instrumental limitations and safety concerns.

Stable operation of the symmetrical SOFC was maintained for 32 h (Fig. 6e). The post-test micrographs (Fig. 6f) demonstrate that the Mn09-30GDC electrode microstructure is well preserved after symmetrical SOFC operation. Cross-sectional SEM analysis confirms the absence of delamination or cracking and reveals a uniform distribution of GDC20 and perovskite phases (Fig. S33–S35, Supporting Information). Importantly, the composite electrode largely preserves its nanofibrous morphology after sintering, while the electrolyte grains are homogeneously integrated within the structure. As a result, the electrode retains a continuous porous network and a high density of accessible surface sites, supporting efficient electrochemical operation under cell conditions. In addition, excellent stability was also observed for the $Sm_{0.9}Ba_{0.9}Mn_{1.35}Fe_{0.45}Co_{0.1}Ni_{0.1}O_{5+\delta}$ + 30%GDC20 -based symmetrical LSGM-supported fuel cell, however, the recorded maximum power density was lower, as shown in Fig. S36 (Supporting Information).

**Table 1**
Electrochemical performance comparison of Mn-based electrodes for SOFCs.

| Cell configuration | Peak power density [mW $cm^{-2}$] | Ref. |
|---|---|---|
| $Sm_{0.9}Ba_{0.9}Mn_{1.8}Co_{0.2}O_{5+\delta}$\|LSGM\| $Sm_{0.9}Ba_{0.9}Mn_{1.8}Co_{0.2}O_{5+\delta}$ symmetrical cell | 712 (900 °C)<br>560 (850 °C)<br>426 (800 °C) | [2] |
| $SmBaMn_{1.9}Ti_{0.1}O_{5+\delta}$\|LSGM\|$SmBaMn_{1.9}Ti_{0.1}O_{5+\delta}$ symmetrical cell | 603 (900 °C)<br>420 (850 °C)<br>296 (800 °C) | [6] |
| $SmBaMn_{1.9}Mg_{0.1}O_{5+\delta}$\|LSGM\|$SmBaMn_{1.9}Mg_{0.1}O_{5+\delta}$ symmetrical cell | 596 (900 °C)<br>462 (850 °C)<br>317 (800 °C) | [7] |
| $SmBaMn_2O_{5+\delta}$\|LSGM\|$SmBaMn_2O_{5+\delta}$ symmetrical cell | 565 (900 °C)<br>421 (850 °C)<br>326 (800 °C) | [5] |
| $SmBaMn_2O_{5+\delta}$\|LSGM\|$SmBaMn_2O_{5+\delta}$ infiltrated with Co—Fe catalyst symmetrical cell | 782 (900 °C)<br>647 (850 °C)<br>481 (800 °C) | [5] |
| $Pr_{0.6}Sr_{0.4}Mn_{0.2}Fe_{0.7}Ni_{0.1}O_{3-\delta}$ + GDC10\|LSGM\| $Pr_{0.6}Sr_{0.4}Mn_{0.2}Fe_{0.7}Ni_{0.1}O_{3-\delta}$ + GDC10 symmetrical cell | 702 (800 °C) | [13] |
| $Ca_{1.5}Co_4O_{9+\delta}$\|GDC\|YSZ\|NiO-YSZ anode-supported cell | 1069 (800 °C) | [10] |
| $Sm_{0.9}Ba_{0.9}Mn_{0.9}Fe_{0.9}Co_{0.1}Ni_{0.1}O_{5+\delta}$ + 30%GDC20\| GDC20\|8YSZ\|Ni + 8YSZ anode-supported cell | **1112** (850 °C)<br>**877** (800 °C) | This work |
| $Sm_{0.9}Ba_{0.9}Mn_{0.9}Fe_{0.9}Co_{0.1}Ni_{0.1}O_{5+\delta}$ + 30%GDC20\| LSGM\| $Sm_{0.9}Ba_{0.9}Mn_{0.9}Fe_{0.9}Co_{0.1}Ni_{0.1}O_{5+\delta}$ + 30% GDC20 symmetrical cell | **816** (800 °C) | This work |

## 3. Conclusion

In this work, we establish a rational and scalable strategy for engineering high-performance symmetrical SOFC electrodes through the integration of electrospun nanofiber architectures and controlled multi-element *in situ* exsolution. By tailoring the composition of $Sm_{0.9}Ba_{0.9}Mn_{1.8-x}Fe_xCo_{0.1}Ni_{0.1}O_{5+\delta}$, we demonstrate that Fe incorporation fundamentally alters exsolution and oxidation pathways, enabling the formation of hollow core–shell $Fe_{3-x-y}Ni_xCo_yO_4$ nano-oxides *via* a Kirkendall-type mechanism. Under reducing conditions, uniformly socketed Co–Ni–Fe alloy nanoparticles exsolve and remain partially embedded in the perovskite lattice, ensuring strong metal–support interactions and stability. Upon oxidation, Fe-containing compositions undergo morphology transformation into hollow core–shell spinel nano-oxides without structural degradation of the host perovskite. This adaptive, reversible nanostructuring introduces an additional degree of morphological control beyond conventional exsolution systems. The electrospun nanofiber framework further amplifies these effects by promoting smaller, denser nanoparticles, suppressing grain coarsening, and delivering substantially higher accessible surface area compared to powders. The optimized composite electrode exhibits a low polarization resistance of 0.046 Ω $cm^2$ at 800 °C. Anode-supported cells achieve a peak power density of 1112 mW $cm^{-2}$ at 850 °C with stable 200 h operation, while symmetrical cells deliver 816 mW $cm^{-2}$ at 800 °C, outperforming previously reported Mn-based S-SOFC systems. Collectively, this work demonstrates that coupling nanofiber morphology with multi-element exsolution enables dynamic, morphology-adaptive nanocatalysts and establishes hollow core–shell engineering as a powerful design paradigm for durable, high-power solid oxide electrochemical systems.

## 4. Experimental section

### 4.1. The synthesis of $Sm_{0.9}Ba_{0.9}Mn_{1.8-x}Fe_xCo_{0.1}Ni_{0.1}O_{5+\delta}$ (x = 0, 0.45, 0.9, and 1.35) oxides

The $Sm_{0.9}Ba_{0.9}Mn_{1.8-x}Fe_xCo_{0.1}Ni_{0.1}O_{5+\delta}$ (x = 0, 0.45, 0.9, and 1.35) nanofibers were obtained by the electrospinning method using a Doxa electrospinning device (Doxa Microfluidics S.L.). Stoichiometric amounts of $Sm(NO_3)_3{\cdot}6H_2O$, $Ba(NO_3)_2$, $Fe(NO_3)_3{\cdot}9H_2O$, Co $(NO_3)_2{\cdot}6H_2O$, $Ni(NO_3)_2{\cdot}6H_2O$ (with ≥99.9% purity) and Mn $(NO_3)_2{\cdot}6H_2O$ (with ≥98% purity) were dissolved in *N*,*N*-dimethylformamide (DMF) under stirring on a hot plate at about 40 °C. Then,

polyvinylpyrrolidone (PVP) was added to the previous solutions, which were further stirred overnight to ensure complete dissolution of PVP. The electrospinning process was conducted at a flow rate of 10–20 μL $min^{-1}$ and the voltage of 13–19 kV was applied with a collecting distance of 15 cm. The calcination of nanofibers was conducted at 900 °C in air for 2 h. The reduction was carried out at 900 °C and 800 °C in 5 vol% $H_2$/Ar and pure hydrogen, respectively, each for 2 h. To confirm the redox stability and possibility of dissolution of nanoparticles, nanofibers were heated in air, at 900 °C, for 2 h.

$Sm_{0.9}Ba_{0.9}Mn_{1.8-x}Fe_xCo_{0.1}Ni_{0.1}O_{5+\delta}$ (x = 0, 0.45, 0.9, and 1.35) powders were synthesized by a soft-chemistry technique. Stoichiometric amounts of the aforementioned salts were dissolved separately in distilled water and then mixed with $HNO_3$ solution. In the following steps, citric acid and ethylenediaminetetraacetic acid were added during stirring in relation to the total amount of all cations at a molar ratio of 1:1 and 1.5:1, respectively. Additionally, ammonia solution was added to neutralize the solutions to a pH value of ~7. The obtained homogeneous solutions were slowly heated to evaporate water, decompose excessive ammonia nitrates, and oxidize residual carbon and nitrogen from organic acids. After milling, the synthesis conditions of the well-mixed $Sm_{0.9}Ba_{0.9}Mn_{1.8-x}Fe_xCo_{0.1}Ni_{0.1}O_{5+\delta}$ precursors (x = 0, 0.45, and 0.9) involved firing at 1000 °C, 950 °C and 800 °C for 10 h in air, 5 vol% $H_2$ in argon, and pure hydrogen, respectively. The $Sm_{0.9}Ba_{0.9}Mn_{0.45}Fe_{1.35}Co_{0.1}Ni_{0.1}O_{5+\delta}$ was calcined in air for 12 h at 1200 °C.

### 4.2. Materials characterization and redox stability studies of investigated compounds

The XRD data of the synthesized materials at room temperature (RT) were collected using a PANalytical Empyrean diffractometer in the 10–100 deg. range with Cu Kα radiation. The diffraction data were refined with the Rietveld method using the GSAS/EXPGUI set of software [99,100]. The average crystallite size of the perovskite phase was calculated using Scherrer's equation $D = \frac{k \bullet \lambda}{\beta \bullet \cos\theta}$, where k, $\lambda$, $\beta$ and $\theta$ are the shape factor (taken as 0.9), the X-ray wavelength (0.154059 nm), the full width at half maximum (°) and the Bragg angle of the peak (°), respectively [101]. For the notation of space groups, the Hermann-Mauguin symbolism (H-M international notation) was used. High-temperature XRD (HT-XRD) measurements were performed on PANalytical Empyrean apparatus equipped with Anton Paar HTK 1200 N oven chamber, from RT to 1000 °C. The HT-XRD data with refinements allowed for the calculation of thermal expansion coefficients (TEC). Raman spectra were recorded in the range of RT to 600 °C using a Thermo Scientific DXR3 Raman Microscope equipped with a laser with an emission wavelength of 532 nm and temperature control stage Linkam THMS600, in the measurement range 50–1870 $cm^{-1}$, and laser power 1 mW.

The Scanning Electron Microscopy (SEM) studies were performed using Field emission type SEM JSM-7100F and ThermoFisher Scientific Apreo 2 SEM. The TEM investigations were performed on an analytical electron microscope JEM-ARM 200F operated at 200 kV, endowed with EDX spectrometer.

Thermal expansion studies were also conducted for the materials studied in air and in 5 vol% $H_2$/Ar up to 900 °C on Linseis L75 Platinum Series dilatometer. Thermogravimetric (TG) measurements were performed on TA Q5000 IR (TA Instruments) from 50 °C to 1000 °C, with a heating rate of 1° $min^{-1}$. For TG-based calculations, the buoyancy effect was taken into account. The determination of the specific surface area of the powders was performed using the Brunauer-Emmett-Teller (BET) technique with the BELSORP II mini (MicrotracBEL Corp.) apparatus.

The chemical stability of the materials under strong reducing conditions was analyzed by annealing the oxides at 800 °C for 10 h in pure hydrogen. After the heat treatment, successive XRD measurements were performed. The compatibility studies of the obtained oxides with commonly used solid electrolytes: GDC20 ($Ce_{0.8}Gd_{0.2}O_{1.9}$), LSGM ($La_{0.8}Sr_{0.2}Ga_{0.8}Mg_{0.2}O_{3-\delta}$) and 8YSZ (8 mol% yttria-stabilized zirconia) were evaluated by analyzing the collected XRD data for the respective mixtures of electrode material and electrolyte powder (50:50 wt%), which were heated at 800 °C in air and 5 vol% $H_2$/Ar for 100 h.

The total electrical conductivity data were collected with the linear 4-probe DC method within a temperature range of 25 − 850 °C, using the Fine Instruments FRASB-1000 apparatus containing TF1200 tube furnace, Keysight Multimeter 34465 A, Keysight Function/Arbitrary Waveform Generator 33210 A, control unit CFRASB-1000 with AM16/32B multiplexer, measuring probe SSC-15 and BR07 retaining decade. The activation energy was calculated using an Arrhenius-type equation for conductivity.

The detailed chemical composition of samples was analyzed by X-ray photoemission spectroscopy (XPS). XPS measurements were performed using Omicron NanoScience equipment. Samples were measured at room temperature, under the ultra-high vacuum conditions and pressures below $1.1 \times 10^{-8}$ mBar. The photoelectrons were excited by a Mg-Kα x-ray source operated at 15 kV and 300 *W*. *Argus* hemispherical spectrophotometer equipped with 128 channel detector was used for photoelectrons energy measurements. The data analysis was performed with the CASA XPS software, using Shirley background subtraction. Curve fitting was carried out using a Gauss-Lorentz curve -GL(30) within a least-squares optimization procedure. The spectra were fitted by minimizing the standard deviation of the residuals between the experimental signal and the fitted model. For each spectral region, the FWHM values and the energy separations between the maxima corresponding to different chemical states were constrained and kept fixed during the fitting procedure to maintain physical consistency of the model.

### 4.3. Quantum mechanical calculations

All first-principles calculations were conducted using the Vienna *Ab initio* Simulation Package (VASP) [102] on 2 × 3 × 2 supercells containing 216 and 236 atoms for $SmBaMn_{2-x}Fe_xO_{6+\delta}$ (x = 0, 0.5, and 1) and $Sm_{0.9}Ba_{0.9}Mn_{1.8-x}Fe_xCo_{0.1}Ni_{0.1}O_{5+\delta}$ (x = 0, 0.45, and 0.90), respectively. The Perdew–Burke–Ernzerhof (PBE) exchange-correlation functional [103], projector-augmented-wave (PAW) potentials, and a plane-wave cutoff energy of 450 eV were employed. Brillouin zone integrations were performed at the Γ point for structural relaxations and phonon computations, and on a 4 × 4 × 4 k-point mesh for static and electronic structure calculations. To correct for the over-delocalization of d-electrons, on-site Coulomb interactions were treated using the Dudarev formalism [104], with effective U values of 6, 7, 8, and 6 eV for Mn, Fe, Ni, and Co, respectively. These parameters were determined by comparing the electronic density of states (DOS) calculated using the HSE06 hybrid functional and the GGA + U approach for different U values. The chosen parameters yielded DOS profiles in closest agreement with the HSE06 results. All calculations included spin polarization to account for magnetic effects. To capture configurational variability, thirty independent supercells were generated for each composition, each with distinct initial occupations of Mn, Fe, Co, and Ni on the available crystallographic sites. The lattice energies obtained from these configurations were used to compute Boltzmann-weighted scaling factors to evaluate the propensity for atomic clustering. Both electronic structure and phonon calculations were performed on the configurations exhibiting the lowest lattice energies.

### 4.4. Construction and measurements of fuel cells

Symmetrical electrolyte-supported fuel cells were prepared based on LSGM electrolytes. LSGM electrolyte pellets were manufactured through air sintering at 1425 °C for 8 h. These pellets were formed under approximately 100 MPa uniaxial pressure using well-ground electrolyte powder mixed with 1 wt% of a poly(-vinyl butyral-*co*-vinyl alcohol-co-vinyl acetate) additive. Electrolytes were polished down to the

thickness of *ca.* 300 μm with the use of a Struers Labopol-30 MD-Piano 220 diamond polishing plate. The anode-supported fuel cell was prepared by flow casting and screen printing of GDC20. The GDC20 buffer layer was sintered in air at 1250 °C for 3 h.

To prepare electrode slurry, the electrode-electrolyte composites were ground in a mortar for 15 min and then mixed with organic binder (terpineol-based 311,237 ink, FuelCellMaterials) in a weight ratio of 2:1. The freshly prepared electrode mixture was screen-printed on the selected electrolyte, with 3 layers on each side and sintered at 850 °C for 2 h. The current collector was made of silver paste (FuelCellMaterials) in the form of a mesh pattern on both sides of the cell and annealed at 700 °C for 30 min. SOFC performance was characterized by using the Solartron SI 1287 electrochemical interface and Solartron 1252 A frequency response analyzer. Impedance spectroscopy studies were executed under open-circuit conditions in the 0.1 Hz – 1 MHz range with an amplitude of 25 mV. The total interfacial polarization resistances ($Rp = R_{HF} + R_{LF}$) were refined corresponding to the equivalent circuits of L-$R_{ohm}$-$(RQ)_{HF}$-$(RQ)_{LF}$, where L represents inductance, R resistance, Q capacitive constant phase element, HF high-frequency contributions, and LF low-frequency contributions. The Distribution of Relaxation Times (DRT) analysis of the corresponding electrochemical impedance spectra (EIS) was performed using DRTtools Matlab script developed by Ciucci's group [105].

## CRediT authorship contribution statement

**Jakub Lach:** Writing – original draft, Visualization, Validation, Software, Project administration, Methodology, Investigation, Formal analysis, Data curation, Conceptualization. **Kun Zheng:** Writing – review & editing, Writing – original draft, Visualization, Supervision, Software, Resources, Project administration, Methodology, Investigation, Funding acquisition, Formal analysis, Conceptualization. **Cristian Radu:** Methodology, Investigation. **Marcin Kryński:** Methodology, Investigation. **Michał Gogacz:** Methodology, Investigation. **Yihan Ling:** Methodology, Investigation. **Alicja Klimkowicz:** Methodology, Investigation. **Marcin Łapiński:** Methodology, Investigation.

## Declaration of competing interest

The authors declare that they have no known competing financial interests or personal relationships that could have appeared to influence the work reported in this paper.

The authors declare the following financial interests/personal relationships which may be considered as potential competing interests: The work is funded by the National Science Centre Poland (NCN) based on the decision number UMO-2021/43/D/ST5/00824. Authors also acknowledge the financial support of research project supported by the program "Excellence Initiative – Research University" for the AGH University of Krakow.

HR-TEM, EDX and SAED results were a part of CERIC-ERIC grant no. 20232033 and were conducted in National Institute of Materials Physics, Măgurele in Romania. Raman spectroscopy measurements were conducted on the apparatus purchased with financial support from the AGH Excellence Initiative - Research University program (IDUB AGH, Action 8).

## Acknowledgements

The work is funded by the National Science Centre Poland (NCN) based on the decision number UMO-2021/43/D/ST5/00824.

Authors also acknowledge the financial support of research project supported by the program "Excellence Initiative – Research University" for the AGH University of Krakow.

HR-TEM, EDX and SAED results were a part of CERIC-ERIC grant no. 20232033 and were conducted in National Institute of Materials Physics, Măgurele in Romania.

Raman spectroscopy measurements were conducted on the apparatus purchased with financial support from the AGH Excellence Initiative - Research University program (IDUB AGH, Action 8).

## Appendix A. Supplementary data

Supplementary data to this article can be found online at https://doi.org/10.1016/j.cej.2026.174527.

## Data availability

Data will be made available on request.

## References

[1] K. Kousi, D. Neagu, L. Bekris, E. Calì, G. Kerherve, E.I. Papaioannou, D.J. Payne, I. S. Metcalfe, Low temperature methane conversion with perovskite-supported: exo/endo -particles, J. Mater. Chem. A Mater. 8 (2020) 12406–12417, https://doi.org/10.1039/d0ta05122e.

[2] Y. Zhang, H. Zhao, M. Zhang, Z. Du, W. Guan, S.C. Singhal, K. Swierczek, Boosting the Electrode Reaction Kinetics of SSOFCs by the Synergistic Effect of Nanoparticle Codecoration on Both the Cathode and Anode, Chem. Mater. 35 (2023) 499–510, https://doi.org/10.1021/acs.chemmater.2c02861.

[3] J. Wang, Z. Chen, M. Li, M. Rao, R. Li, X. Ou, Y. Tian, F. Jin, C. Shen, Y. Ling, Different alkaline earth metals doped $Sm_{0.5}A_{0.5}Fe_{0.9}Ni_{0.1}O_{3-\delta}$ (A=Ca, Sr and Ba) for symmetric solid oxide fuel cells, Int. J. Hydrog. Energy 48 (2023) 10203–10214, https://doi.org/10.1016/j.ijhydene.2022.12.117.

[4] A.M. Abdalla, S. Hossain, P.M.I. Petra, C.D. Savaniu, J.T.S. Irvine, A.K. Azad, Novel layered perovskite $SmBaMn_2O_{5+\delta}$ for SOFCs anode material, Mater. Lett. 204 (2017) 129–132, https://doi.org/10.1016/j.matlet.2017.06.029.

[5] Y. Zhang, H. Zhao, Z. Du, K. Świerczek, Y. Li, High-Performance $SmBaMn_2O_{5+\delta}$ Electrode for Symmetrical Solid Oxide Fuel Cell, Chem. Mater. 31 (2019) 3784–3793, https://doi.org/10.1021/acs.chemmater.9b01012.

[6] Y. Zhang, H. Zhao, M. Zhang, T. Yang, Z. Du, Development of titanium-doped $SmBaMn_2O_{5+\delta}$ layered perovskite as a robust electrode for symmetrical solid oxide fuel cells, Int. J. Hydrog. Energy 48 (2023) 28119–28130, https://doi.org/10.1016/j.ijhydene.2023.03.388.

[7] Y. Zhang, B. Zhang, H. Zhao, K. Świerczek, Z. Du, Y. Li, L. Xu, H. Li, Electrochemical performance and structural durability of Mg-doped $SmBaMn_2O_{5+\delta}$ layered perovskite electrode for symmetrical solid oxide fuel cell, Catal. Today 364 (2021) 80–88, https://doi.org/10.1016/j.cattod.2020.05.057.

[8] D. Liu, Z. Chen, W. Zhang, M. Sun, F. Jin, H. Liu, X. Ou, K. Zheng, Y. Ling, One-pot fabrication of high-entropy heterostructure cathode materials with excellent anti-poisoning properties in solid oxide fuel cells, J. Power Sources 626 (2025) 235809, https://doi.org/10.1016/j.jpowsour.2024.235809.

[9] W. Zhang, H. Wang, X. Chen, X. Liu, J. Meng, Manipulation of rare earth on voltage-driven in-situ exsolution process of perovskite cathodes for low-temperature solid oxide fuel cells, Chem. Eng. J. 446 (2022) 136934, https://doi.org/10.1016/j.cej.2022.136934.

[10] X. Wu, Y. Tian, Y. Zhang, W. Guo, Y. Li, J. Zhu, L. Wang, Promotion of $Ca_3Co_4O_{9+\delta}$ oxygen electrode by in-situ exsolution of nanoparticles for solid oxide cells, Int. J. Hydrog. Energy 50 (2024) 1246–1254, https://doi.org/10.1016/j.ijhydene.2023.10.222.

[11] O.L. Pineda, Z.L. Moreno, P. Roussel, K. Świerczek, G.H. Gauthier, Synthesis and preliminary study of the double perovskite $NdBaMn_2O_{5+\delta}$ as symmetric SOFC electrode material, Solid State Ionics 288 (2016) 61–67, https://doi.org/10.1016/j.ssi.2016.01.022.

[12] S. Durán, N. Rangel, C. Silva, M.A. Macias, E. Capoen, C. Pirovano, A. Niemczyk, L. Suescun, P. Roussel, G.H. Gauthier, Study of $La_4BaCu_{5-x}Mn_xO_{13+\delta}$ materials as potential electrode for symmetrical-SOFC, Solid State Ionics 341 (2019) 115031, https://doi.org/10.1016/j.ssi.2019.115031.

[13] J. Choi, D. Jang, M. Kim, J. Ha, H. Ahn, W.B. Kim, Multi-functional perovskite oxide $Pr_{0.6}Sr_{0.4}Mn_{0.2}Fe_{0.7}Ni_{0.1}O_{3-\delta}$ as an efficient quasi-symmetric electrode for solid oxide fuel/electrolysis cells, J. Mater. Chem. A Mater. 12 (2024) 12619–12627, https://doi.org/10.1039/d3ta08110a.

[14] J. Lach, K. Zheng, M. Gogacz, P. Czaja, J. Luo, A. Brzoza-Kos, Electrospun Nanofiber Electrodes with *in situ* Exsolved Nanocatalysts for Symmetrical SOCs, ECS Trans. 111 (2023) 1025–1034, https://doi.org/10.1149/11106.1025ecst.

[15] Y. Tian, C. Yang, Y. Wang, M. Xu, Y. Ling, J. Pu, F. Ciucci, J.T.S. Irvine, B. Chi, Phase transition with *in situ* exsolution nanoparticles in the reduced $Pr_{0.5}Ba_{0.5}Fe_{0.8}Ni_{0.2}O_{3-\delta}$ electrode for symmetric solid oxide cells, J. Mater. Chem. A Mater. 10 (2022) 16490–16496, https://doi.org/10.1039/d2ta03395j.

[16] N. Hou, T. Yao, P. Li, X. Yao, T. Gan, L. Fan, J. Wang, X. Zhi, Y. Zhao, Y. Li, A-site ordered double perovskite with *in situ* exsolved core-shell nanoparticles as anode for solid oxide fuel cells, ACS Appl. Mater. Interfaces 11 (2019) 6995–7005, https://doi.org/10.1021/acsami.8b19928.

[17] S. Sengodan, S. Choi, A. Jun, T.H. Shin, Y.W. Ju, H.Y. Jeong, J. Shin, J.T.S. Irvine, G. Kim, Layered oxygen-deficient double perovskite as an efficient and stable anode for direct hydrocarbon solid oxide fuel cells, Nat. Mater. 14 (2015) 205–209, https://doi.org/10.1038/nmat4166.

[18] A. Klimkowicz, K. Świerczek, A. Takasaki, J. Molenda, B. Dabrowski, Crystal structure and oxygen storage properties of $BaLnMn_2O_{5+\delta}$ (Ln: Pr, Nd, Sm, Gd, Dy,

Er and Y) oxides, Mater. Res. Bull. 65 (2015) 116–122, https://doi.org/10.1016/j.materresbull.2015.01.041.
[19] M. Gilleßen, M. Lumeij, J. George, R. Stoffel, T. Motohashi, S. Kikkawa, R. Dronskowski, Oxygen-storage materials $BaYMn_2O_{5+\delta}$ from the quantum-chemical point of view, Chem. Mater. 24 (2012) 1910–1916, https://doi.org/10.1021/cm300655y.
[20] A. Klimkowicz, K. Świerczek, K. Zheng, M. Baranowska, A. Takasaki, B. Dabrowski, Evaluation of $BaY_{1-x}Pr_xMn_2O_{5+\delta}$ oxides for oxygen storage technology, Solid State Ionics 262 (2014) 659–663, https://doi.org/10.1016/j.ssi.2013.11.001.
[21] K. Zheng, Enhanced oxygen mobility by doping Yb in $BaGd_{1-x}Yb_xMn_2O_{5+\delta}$ double perovskite-structured oxygen storage materials, Solid State Ionics 335 (2019) 103–112, https://doi.org/10.1016/j.ssi.2019.03.001.
[22] F. Tonus, M. Bahout, V. Dorcet, R.K. Sharma, E. Djurado, S. Paofai, R.I. Smith, S. J. Skinner, A-site order-disorder in the $NdBaMn_2O_{5+\delta}$ SOFC electrode material monitored in situ by neutron diffraction under hydrogen flow, J. Mater. Chem. A Mater. 5 (2017) 11078–11085, https://doi.org/10.1039/c7ta01439b.
[23] A.A. Taskin, A.N. Lavrov, Y. Ando, Fast oxygen diffusion in A-site ordered perovskites, Prog. Solid State Chem. 35 (2007) 481–490, https://doi.org/10.1016/j.progsolidstchem.2007.01.014.
[24] A.A. Taskin, A.N. Lavrov, Y. Ando, Achieving fast oxygen diffusion in perovskites by cation ordering, Appl. Phys. Lett. 86 (2005) 1–3, https://doi.org/10.1063/1.1864244.
[25] A.C. Tomkiewicz, M.A. Tamimi, A. Huq, S. McIntosh, Structural analysis of $PrBaMn_2O_{5+\delta}$ under SOFC anode conditions by in-situ neutron powder diffraction, J. Power Sources 330 (2016) 240–245, https://doi.org/10.1016/j.jpowsour.2016.09.013.
[26] J. Choi, S. Park, H. Han, M. Kim, M. Park, J. Han, W.B. Kim, Highly efficient $CO_2$ electrolysis to CO on Ruddlesden-Popper perovskite oxide with *in situ* exsolved Fe nanoparticles, J. Mater. Chem. A Mater. 9 (2021) 8740–8748, https://doi.org/10.1039/d0ta11328j.
[27] J. Ha, J. Choi, J. Maeng, G.H. Park, J. Ji, S. Choi, N. Kim, S. Jeong, W.B. Kim, Lattice-controlled Fe-exsolved perovskite anodes for high-performance and durable ammonia-powered electrochemical systems, Chem. Eng. J. 522 (2025) 168167, https://doi.org/10.1016/j.cej.2025.168167.
[28] C. Ni, J. Zhou, Z. Zhang, S. Li, J. Ni, K. Wu, J.T.S. Irvine, Iron-based electrode materials for solid oxide fuel cells and electrolysers, Energy Environ. Sci. 14 (2021) 6287–6319, https://doi.org/10.1039/d1ee01420j.
[29] J. Lach, M. Gogacz, P. Winiarz, Y. Ling, M. Zhou, K. Zheng, A Review of Nanofiber Electrodes and the In Situ Exsolution of Nanoparticles for Solid Oxide Cells, Materials 18 (2025) 1272, https://doi.org/10.3390/ma18061272.
[30] M. Qin, Y. Xiao, H. Yang, T. Tan, Z. Wang, X. Fan, C. Yang, Ru/Nb co-doped perovskite anode: Achieving good coking resistance in hydrocarbon fuels via core-shell nanocatalysts exsolution, Appl. Catal. B 299 (2021) 120613, https://doi.org/10.1016/j.apcatb.2021.120613.
[31] T. Tan, Z. Wang, M. Qin, W. Zhong, J. Hu, C. Yang, M. Liu, *In Situ* Exsolution of Core-Shell Structured $NiFe/FeO_x$ Nanoparticles on $Pr_{0.4}Sr_{1.6}(NiFe)_{1.5}Mo_{0.5}O_{6-\delta}$ for $CO_2$ Electrolysis, Adv. Funct. Mater. 32 (2022) 2202878, https://doi.org/10.1002/adfm.202202878.
[32] K. Kim, S. Joo, R. Huang, H.J. Kim, G. Kim, J.W. Han, Mechanistic insights into the phase transition and metal ex-solution phenomena of $Pr_{0.5}Ba_{0.5}Mn_{0.85}Co_{0.15}O_{3-\delta}$ from simple to layered perovskite under reducing conditions and enhanced catalytic activity, Energy Environ. Sci. 14 (2021) 873–882, https://doi.org/10.1039/d0ee02875d.
[33] K. Kousi, C. Tang, I.S. Metcalfe, D. Neagu, Emergence and Future of Exsolved Materials, Small 17 (2021) 2006479, https://doi.org/10.1002/smll.202006479.
[34] M. Santaya, H.E. Troiani, A. Caneiro, L.V. Mogni, Ternary Ni−Co−Fe exsolved nanoparticles/perovskite system for energy applications: Nanostructure characterization and electrochemical activity, ACS Appl. Energy Mater. 3 (2020) 9528–9533, https://doi.org/10.1021/acsaem.0c01997.
[35] C. Li, Y. Deng, L. Yang, B. Liu, D. Yan, L. Fan, J. Li, L. Jia, An active and stable hydrogen electrode of solid oxide cells with exsolved Fe–Co–Ni nanoparticles from $Sr_2FeCo_{0.2}Ni_{0.2}Mo_{0.6}O_{6-\delta}$ double-perovskite, Advanced Powder Materials 2 (2023) 100133, doi:https://doi.org/10.1016/j.apmate.2023.100133.
[36] A.K. Opitz, A. Nenning, V. Vonk, S. Volkov, F. Bertram, H. Summerer, S. Schwarz, A. Steiger-Thirsfeld, J. Bernardi, A. Stierle, J. Fleig, Understanding electrochemical switchability of perovskite-type exsolution catalysts, Nat. Commun. 11 (2020) 1–10, https://doi.org/10.1038/s41467-020-18563-w.
[37] F.N. Agüero, A.M. Beltrán, M.A. Fernández, L.E. Cadús, Surface nickel particles generated by exsolution from a perovskite structure, J. Solid State Chem. 273 (2019) 75–80, https://doi.org/10.1016/j.jssc.2019.02.036.
[38] H. Han, J. Park, S.Y. Nam, K.J. Kim, G.M. Choi, S.S.P. Parkin, H.M. Jang, J.T. S. Irvine, Lattice strain-enhanced exsolution of nanoparticles in thin films, Nat. Commun. 10 (2019) 1471, https://doi.org/10.1038/s41467-019-09395-4.
[39] B. Rudolph, A.I. Tsiotsias, B. Ehrhardt, P. Dolcet, S. Gross, S. Haas, N.D. Charisou, M.A. Goula, S. Mascotto, Nanoparticle Exsolution from Nanoporous Perovskites for Highly Active and Stable Catalysts, Adv. Sci. 10 (2023) 2205890, https://doi.org/10.1002/advs.202205890.
[40] M. Xu, R. Cao, S. Wu, J.G. Lee, D. Chen, J.T.S. Irvine, Nanoparticle exsolution via electrochemical switching in perovskite fibers for solid oxide fuel cell electrodes, J. Mater. Chem. A Mater. 11 (2023) 13007–13015, https://doi.org/10.1039/d3ta00535f.
[41] S. Jo, Y. Han Kim, H. Jeong, C. ho Park, B.R. Won, H. Jeon, K. Taek Lee, J. ha Myung, Exsolution of phase-separated nanoparticles via trigger effect toward reversible solid oxide cell, Appl Energy 323 (2022) 119615, https://doi.org/10.1016/j.apenergy.2022.119615.
[42] M. Najimu, S. Jo, K.L. Gilliard-AbdulAziz, Co-Exsolution of Ni-Based Alloy Catalysts for the Valorization of Carbon Dioxide and Methane, Acc. Chem. Res. 56 (2023) 3132–3141, https://doi.org/10.1021/acs.accounts.3c00404.
[43] D. Jennings, S. Ricote, J. Santiso, J. Caicedo, I. Reimanis, Effects of exsolution on the stability and morphology of Ni nanoparticles on BZY thin films, Acta Mater. 228 (2022) 117752, https://doi.org/10.1016/j.actamat.2022.117752.
[44] J. Xia, C. Wang, X. Wang, L. Bi, Y. Zhang, A perspective on DRT applications for the analysis of solid oxide cell electrodes, Electrochim. Acta 349 (2020) 136328, https://doi.org/10.1016/j.electacta.2020.136328.
[45] S.T. Aruna, L.S. Balaji, S.S. Kumar, B.S. Prakash, Electrospinning in solid oxide fuel cells – A review, Renew. Sust. Energ. Rev. 67 (2017) 673–682, https://doi.org/10.1016/j.rser.2016.09.003.
[46] J. Bai, Z. Han, B. Lv, X. Chen, X. Zhu, D. Zhou, Preparation of 3D structure high performance $Ba_{0.5}Sr_{0.5}Fe_{0.8}Cu_{0.2}O_{3-\delta}$ nanofiber SOFC cathode material by low-temperature calcination method, Int. J. Hydrog. Energy 46 (2021) 8132–8142, https://doi.org/10.1016/j.ijhydene.2020.11.263.
[47] C.L. Chang, C.S. Hsu, J.B. Huang, P.H. Hsu, B.H. Hwang, Preparation and characterization of SOFC cathodes made of SSC nanofibers, J. Alloys Compd. 620 (2015) 233–239, https://doi.org/10.1016/j.jallcom.2014.09.131.
[48] M. Ahn, S. Han, J. Lee, W. Lee, Electrospun composite nanofibers for intermediate-temperature solid oxide fuel cell electrodes, Ceram. Int. 46 (2020) 6006–6011, https://doi.org/10.1016/j.ceramint.2019.11.057.
[49] M. Ahn, J. Cho, W. Lee, One-step fabrication of composite nanofibers for solid oxide fuel cell electrodes, J. Power Sources 434 (2019) 226749, https://doi.org/10.1016/j.jpowsour.2019.226749.
[50] S.J. Kim, M. Choi, T. Mun, D.Y. Woo, W. Lee, Infiltrated Nanofiber-Based Nanostructured Electrodes for Solid Oxide Fuel Cells, Int. J. Energy Res. 2023 (2023) 410245, https://doi.org/10.1155/2023/7410245.
[51] Y. Sun, S. Dai, High-entropy materials for catalysis: A new frontier, Sci. Adv. 7 (2021) 1–23, https://doi.org/10.1126/sciadv.abg1600.
[52] V. Chapman, B.J. Welch, M. Skyllas-Kazacos, High temperature oxidation behaviour of Ni-Fe-Co anodes for aluminium electrolysis, Corros. Sci. 53 (2011) 2815–2825, https://doi.org/10.1016/j.corsci.2011.05.018.
[53] G.D. Park, J.S. Cho, Y.C. Kang, Multiphase and Double-Layer $NiFe_2O_4$@NiO Hollow-Nanosphere-Decorated Reduced Graphene Oxide Composite Powders Prepared by Spray Pyrolysis Applying Nanoscale Kirkendall Diffusion, ACS Appl. Mater. Interfaces 7 (2015) 16842–16849, https://doi.org/10.1021/acsami.5b04891.
[54] A. Kaczmarska, Z. Grzesik, S. Mrowec, On the defect structure and transport properties of $Co_3O_4$ spinel oxide, High Temp. Mater. Processes 31 (2012) 371–379, https://doi.org/10.1515/htmp-2012-0069.
[55] X. Geng, M. Vega-Paredes, Z. Wang, C. Ophus, P. Lu, Y. Ma, S. Zhang, C. Scheu, C. H. Liebscher, B. Gault, Grain boundary engineering for efficient and durable electrocatalysis, Nat. Commun. 15 (2024) 8534, https://doi.org/10.1038/s41467-024-52919-w.
[56] W. Fan, Z. Sun, Y. Bai, K. Wu, J. Zhou, Y. Cheng, *In situ* growth of nanoparticles in A-site deficient ferrite perovskite as an advanced electrode for symmetrical solid oxide fuel cells, J. Power Sources 456 (2020) 228000, https://doi.org/10.1016/j.jpowsour.2020.228000.
[57] M. Xu, Y. Jeon, A. Naden, H. Kim, G. Kerherve, D.J. Payne, Y.G. Shul, J.T. S. Irvine, Synergistic growth of nickel and platinum nanoparticles via exsolution and surface reaction, Nat. Commun. 15 (2024) 4007, https://doi.org/10.1038/s41467-024-48455-2.
[58] J. Zhou, J. Yang, Z. Zong, L. Fu, Z. Lian, C. Ni, J. Wang, Y. Wan, K. Wu, A mesoporous catalytic fiber architecture decorated by exsolved nanoparticles for reversible solid oxide cells, J. Power Sources 468 (2020) 228349, https://doi.org/10.1016/j.jpowsour.2020.228349.
[59] L. Fu, J. Zhou, L. Zhou, J. Yang, Z. Liu, K. Wu, H. Zhao, J. Wang, K. Wu, Facile fabrication of exsolved nanoparticle-decorated hollow ferrite fibers as active electrocatalyst for oxygen evolution reaction, Chem. Eng. J. 418 (2021) 129422, https://doi.org/10.1016/j.cej.2021.129422.
[60] D. Neagu, G. Tsekouras, D.N. Miller, H. Ménard, J.T.S. Irvine, *In situ* growth of nanoparticles through control of non-stoichiometry, Nat. Chem. 5 (2013) 916–923, https://doi.org/10.1038/nchem.1773.
[61] K. Zheng, J. Lach, H. Zhao, X. Huang, K. Qi, Magnesium-Doped $Sr_2(Fe,Mo)O_{6-\delta}$ Double Perovskites with Excellent Redox Stability as Stable Electrode Materials for Symmetrical Solid Oxide Fuel Cells, Membranes 12 (2022) 1006, doi:https://doi.org/10.3390/membranes12101006.
[62] Y. Ueda, T. Nakajima, Novel structures and electromagnetic properties of the A-site-ordered/disordered manganites $RBaMn_2O_6/R_{0.5}Ba_{0.5}MnO_3$ (R = Y and rare earth elements), Journal of Physics Condensed Matter. 16 (2004) S573, DOI: https://doi.org/10.1088/0953-8984/16/11/002.
[63] D. Zhang, Y. Shi, H. Zhao, W. Qi, X. Chen, T. Zhan, S. Li, B. Yang, M. Sun, J. Lai, B. Huang, L. Wang, The facile oil-phase synthesis of a multi-site synergistic high-entropy alloy to promote the alkaline hydrogen evolution reaction, J. Mater. Chem. A Mater. 9 (2021) 889–893, https://doi.org/10.1039/d0ta10574k.
[64] B. Hua, Y.F. Sun, M. Li, N. Yan, J. Chen, Y.Q. Zhang, Y. Zeng, B. Shalchi Amirkhiz, J.L. Luo, Stabilizing Double Perovskite for Effective Bifunctional Oxygen Electrocatalysis in Alkaline Conditions, Chem. Mater. 29 (2017) 6228–6237, https://doi.org/10.1021/acs.chemmater.7b01114.
[65] S. Bernardini, F. Bellatreccia, A. Casanova Municchia, G. Della Ventura, A. Sodo, Raman spectra of natural manganese oxides, J. Raman Spectrosc. 50 (2019) 873–888, https://doi.org/10.1002/jrs.5583.
[66] E. Kroumova, M.I. Aroyo, J.M. Perez-Mato, A. Kirov, C. Capillas, S. Ivantchev, H. Wondratschek, Bilbao Crystallographic Server: Useful Databases and Tools for

Phase Transition Studies, Phase Transitions: A Multinational Journal 76 (2003) 155–170, https://doi.org/10.1080/0141159031000076110.
[67] P. Thakur, K.I. Nassar, D. Kumar, P. Kumar, P. Sharma, V. Tirth, A.S. Alosaimy, A. Algahtani, M. Essid, M. Lal, Tailoring of structural, morphological, electrical, and magnetic properties of $LaMn_{1-x}Fe_xO_3$ ceramics, RSC Adv. 14 (2024) 23592–23605, https://doi.org/10.1039/d4ra04931d.
[68] M.P. Zahler, S.M. Kraschewski, H. Störmer, D. Gerthsen, M. Bäurer, W. Rheinheimer, Grain growth and segregation in Fe-doped $SrTiO_3$: Experimental evidence for solute drag, J. Eur. Ceram. Soc. 43 (2023) 1613–1624, https://doi.org/10.1016/j.jeurceramsoc.2022.11.074.
[69] S. Singh, D. Singh, Structural, magnetic and electrical properties of Fe-doped perovskite manganites $La_{0.8}Ca_{0.15}Na_{0.05}Mn_{1-x}Fe_xO_3$ (x = 0, 0.05, 0.10 and 0.15), J. Alloys Compd. 702 (2017) 249–257, https://doi.org/10.1016/j.jallcom.2017.01.154.
[70] M.L. Weber, M. Kindelmann, D. Jennings, J. Hölschke, R. Dittmann, J. Mayer, W. Rheinheimer, X. Fang, F. Gunkel, Atomic-Scale Insights into Nanoparticle Exsolution at Dislocations in Dislocation-Engineered Catalysts, Adv. Mater. 38 (2025) e02362, https://doi.org/10.1002/adma.202502362.
[71] H. Jeong, Y.H. Kim, B.R. Won, H. Jeon, C.H. Park, J.H. Myung, Emerging Exsolution Materials for Diverse Energy Applications: Design, Mechanism, and Future Prospects, Chem. Mater. 35 (2023) 3745–3764, https://doi.org/10.1021/acs.chemmater.3c00004.
[72] Y.H. Kim, Y. Kang, S. Jo, H. Jeong, D. Neagu, J. ha Myung, Shape-shifting nanoparticles on a perovskite oxide for highly stable and active heterogeneous catalysis, Chem. Eng. J. 441 (2022) 136025, https://doi.org/10.1016/j.cej.2022.136025.
[73] O. Kwon, S. Sengodan, K. Kim, G. Kim, H. Young Jeong, J. Shin, Y.-W. Ju, J. Woo Han, G. Kim, Exsolution trends and co-segregation aspects of self-grown catalyst nanoparticles in perovskites, Nat. Commun. 8 (2017) 15967, https://doi.org/10.1038/ncomms15967.
[74] K. Zheng, J. Lach, P. Czaja, M. Gogacz, P. Czach, A. Brzoza-Kos, P. Winiarz, J. Luo, Designing high-performance quasi-symmetrical solid oxide cells with a facile chemical modification strategy for $Sr_2Fe_{2-x}W_xO_{6-\delta}$ ferrites electrodes with *in situ* exsolution of nanoparticles, J. Power Sources 587 (2023) 233707, https://doi.org/10.1016/j.jpowsour.2023.233707.
[75] E. Konysheva, E. Suard, J.T.S. Irvine, Effect of oxygen non stoichiometry and oxidation state of transition elements on high-temperature phase transition in a site deficient $La_{0.95}Ni_{0.6}Fe_{0.4}O_{3-\delta}$ perovskite, Chem. Mater. 21 (2009) 5307–5318, https://doi.org/10.1021/cm902443n.
[76] A. Klimkowicz, K. Świerczek, A. Takasaki, B. Dabrowski, Oxygen storage capability in Co- and Fe-containing perovskite-type oxides, Solid State Ionics 257 (2014) 23–28, https://doi.org/10.1016/j.ssi.2014.01.018.
[77] C.L. Muhich, V.J. Aston, R.M. Trottier, A.W. Weimer, C.B. Musgrave, First Principles Analysis of Cation Diffusion in Mixed Metal Ferrite Spinels, Chem. Mater. 28 (2016) 214–226, https://doi.org/10.1021/acs.chemmater.5b03911.
[78] W.L. Roth, The magnetic structure of $Co_3O_4$, J. Phys. Chem. Solids 25 (1964) 1–10, https://doi.org/10.1016/0022-3697(64)90156-8.
[79] P. Saxena, D. Varshney, Effect of d-block element substitution on structural and dielectric properties on iron cobaltite, J. Alloys Compd. 705 (2017) 320–326, https://doi.org/10.1016/j.jallcom.2017.02.120.
[80] K. Verma, A. Kumar, D. Varshney, Dielectric relaxation behavior of $A_xCo_{1-x}Fe_2O_4$ (A = Zn, Mg) mixed ferrites, J. Alloys Compd. 526 (2012) 91–97, https://doi.org/10.1016/j.jallcom.2012.02.089.
[81] L. Zhou, A. Rai, N. Piekiel, X. Ma, M.R. Zachariah, Ion-mobility spectrometry of nickel nanoparticle oxidation kinetics: Application to energetic materials, J. Phys. Chem. C 112 (2008) 16209–16218, https://doi.org/10.1021/jp711235a.
[82] G.C. Wood, I.G. Wright, T. Hodgkiess, D.P. Whittle, A Comparison of the Oxidation of Fe-Cr, Ni-Cr and Co-Cr Alloys in Oxygen and Water Vapour, Mater. Corros. 21 (1970) 900–910, https://doi.org/10.1002/maco.19700211105.
[83] M. Xiao, Z. Liu, H. Di, Y. Bai, G. Yang, D.A. Medvedev, Z. Luo, W. Wang, W. Zhou, R. Ran, Z. Shao, High-entropy materials for solid oxide cells: Synthesis, applications, and prospects, Journal of Energy, Chemistry 104 (2025) 268–296, https://doi.org/10.1016/j.jechem.2024.12.009.
[84] F. Tietz, Thermal Expansion of SOFC Materials, Ionics 5 (1999) 129–139, https://doi.org/10.1007/BF02375916.
[85] H. Ullmann, N. Trofimenko, F. Tietz, D. Stover, A. Ahmad-Khanlou, Correlation between thermal expansion and oxide ion transport in mixed conducting perovskite-type oxides for SOFC cathodes, Solid State Ionics 138 (2000) 79–90, https://doi.org/10.1016/S0167-2738(00)00770-0.
[86] D.W. Smith, An acidity scale for binary oxides, J. Chem. Educ. 64 (1987) 480–481, https://doi.org/10.1021/ed064p480.
[87] W. Xing, Y. Larring, K. Bao, Oxide's Acidity Prediction in Smith Scale Using a Simple Linear Model, Mater. Chem. (2025), https://doi.org/10.26434/chemrxiv-2024-kq9wl-v3.
[88] C. Nicollet, H.L. Tuller, Perspective on the Relationship between the Acidity of Perovskite Oxides and Their Oxygen Surface Exchange Kinetics, Chem. Mater. 34 (2022) 991–997, https://doi.org/10.1021/acs.chemmater.1c03140.
[89] X. Li, H. Zhao, F. Gao, Z. Zhu, N. Chen, W. Shen, Synthesis and electrical properties of Co-doped $Y_{0.08}Sr_{0.92}TiO_{3-\delta}$ as a potential SOFC anode, Solid State Ionics 179 (2008) 1588–1592, https://doi.org/10.1016/j.ssi.2007.12.097.
[90] J.F. Moulder, W.F. Stickle, P.E. Sobol, K.D. Bomben, J. Chastain, Handbook of X-ray Photoelectron Spectroscopy A Reference Book of Standard Spectra for Identification and Interpretation of XPS Data, Physical Electronics Division, Perkin-Elmer Corporation 40 (221) (1992) (ISBN: 0-9648124-1-X).
[91] C.P. Jijil, I.M. Patil, B. Kakade, R. Nandini Devi, Cobalt-Doped $Ba_2In_2O_5$ Brownmillerites: An Efficient Electrocatalyst for Oxygen Reduction in Alkaline Medium, ACS, Omega 3 (2018) 1710–1717, https://doi.org/10.1021/acsomega.7b01655.
[92] K. Świerczek, J. Marzec, D. Pałubiak, W. Zajac, J. Molenda, LFN and LSCFN perovskites - structure and transport properties, Solid State Ionics 177 (2006) 1811–1817, https://doi.org/10.1016/j.ssi.2006.03.038.
[93] A. Chiara, G. Raimondi, R. Merkle, J. Maier, C.V. Bordenca, C. Pipitone, A. Longo, F. Giannici, Interface Diffusion and Compatibility of $(Ba,La)FeO_{3-\delta}$ Perovskite Electrodes in Contact with Barium Zirconate and Ceria, ACS Appl. Mater. Interfaces 15 (2023) 50225–50236, doi:https://doi.org/10.1021/acsami.3c13013.
[94] J.M.S. Skakle, R. Herd, Crystal chemistry of $(RE,A)_2M_3O_7$ compounds (RE=Y, lanthanide; A=Ba, Sr, Ca; M=Al, Ga), Powder Diffract. 14 (1999) 195–202, doi: https://doi.org/10.1017/S0885715600010526.
[95] S.F. Wang, H.C. Lu, Y.F. Hsu, P. Jasinski, High-performance anode-supported solid oxide fuel cells with co-fired $Sm_{0.2}Ce_{0.8}O_{2-\delta}/La_{0.8}Sr_{0.2}Ga_{0.8}Mg_{0.2}O_{3-\delta}/Sm_{0.2}Ce_{0.8}O_{2-\delta}$ sandwiched electrolyte, Int. J. Hydrog. Energy 47 (2022) 5429–5438, https://doi.org/10.1016/j.ijhydene.2021.11.132.
[96] Z. Shao, S.M. Halle, A high-performance cathode for the next generation of solid-oxide fuel cells, Nature 431 (2004) 170–173, https://doi.org/10.1038/nature02863.
[97] A.; Bieberle, L.J. Gauckler, Ni-Based SOFC Anodes: Microstructure and Electrochemistry, Int. J. Mater. Res. 92 (2001) 796–802, doi:https://doi.org/10.3929/ethz-b-000535486.
[98] M.J. Jørgensen, M. Mogensen, Impedance of Solid Oxide Fuel Cell LSM/YSZ Composite Cathodes, J. Electrochem. Soc. 148 (2001) A433, https://doi.org/10.1149/1.1360203.
[99] B.H. Toby, R.B. Von Dreele, GSAS-II (GENERAL STRUCTURE AND ALAYSIS SYSTEM-II), USDOE Office of Science (2023) 102535, doi:10.11578/dc.20230314.2.
[100] B.H. Toby, EXPGUI, a graphical user interface for GSAS, J. Appl. Crystallogr. 34 (2001) 210–213, https://doi.org/10.1107/S0021889801002242.
[101] M.K. Alam, M.S. Hossain, N.M. Bahadur, S. Ahmed, A comparative study in estimating of crystallite sizes of synthesized and natural hydroxyapatites using Scherrer Method, Williamson-Hall model, Size-Strain Plot and Halder-Wagner Method, J. Mol. Struct. 1306 (2024) 137820, https://doi.org/10.1016/j.molstruc.2024.137820.
[102] G. Kresse, Ab initio molecular dynamics for liquid metals, J. Non-Cryst. Solids 192–193 (1995) 222–229, https://doi.org/10.1016/0022-3093(95)00355-X.
[103] J.P. Perdew, K. Burke, M. Ernzerhof, Generalized Gradient Approximation Made Simple, Phys. Rev. Lett. 77 (1996) 3865, https://doi.org/10.1103/PhysRevLett.77.3865.
[104] S.L. Dudarev, G.A. Botton, S.Y. Savrasov, C.J. Humphreys, A.P. Sutton, Electron-energy-loss spectra and the structural stability of nickel oxide: An LSDA+U study, Phys. Rev. B57 (1998) 1505, doi:https://doi.org/10.1103/PhysRevB.57.1505.
[105] T.H. Wan, M. Saccoccio, C. Chen, F. Ciucci, Influence of the Discretization Methods on the Distribution of Relaxation Times Deconvolution: Implementing Radial Basis Functions with DRTtools, Electrochim. Acta 184 (2015) 483–499, https://doi.org/10.1016/j.electacta.2015.09.097.